Human IFT52 mutations uncover a novel role for the protein in microtubule dynamics and centrosome cohesion

Marie Alice Dupont, Camille Humbert, Céline Huber, Quentin Siour, Ida Chiara Guerrera, Vincent Jung, Anni Christensen, Aurore Pouliet, Meriem Garfa-Traore, Patrick Nitschke, et al.

Human *IFT52* mutations uncover a novel role for the protein in microtubule dynamics and centrosome cohesion

Marie Alice Dupont[1,4], Camille Humbert[1,4], Céline Huber[2,3,4], Quentin Siour[2,3,4], Ida Chiara Guerrera[5], Vincent Jung[5], Anni Christensen[6], Aurore Pouliet[7], Meriem Garfa-Traoré[8], Patrick Nitschké[4, 9], Marie Injeyan[10], Kathryn Millar[10], David Chitayat[10,11], Patrick Shannon[12], Katta Mohan Girisha[13], Anju Shukla[13], Charlotte Mechler[14], Esben Lorentzen[6], Alexandre Benmerah[1,4], Valérie Cormier-Daire[2,3,4], Cécile Jeanpierre[1,4], Sophie Saunier[1,4] and Marion Delous[1,4]*

[1]INSERM UMR1163, Laboratory of Hereditary Kidney Diseases, 75015 Paris, France;

[2]INSERM UMR1163, Laboratory of Molecular and Physiopathological bases of osteochondrodysplasia, 75015 Paris, France;

[3]Department of Genetics, Reference Centre for Skeletal Dysplasia, AP-HP, Necker-Enfants Malades Hospital, 75015 Paris, France;

[4]Paris Descartes-Sorbonne Paris Cité University, Imagine Institute, 75015 Paris, France;

[5]Proteomics Platform 3P5-Necker, Paris Descartes-Sorbonne Paris Cité University, Structure Fédérative de Recherche Necker, INSERM US24/CNRS UMS3633, 75015 Paris, France;

[6]Department of Structural Cell Biology, Max-Planck-Institute of Biochemistry, 82152 Martinsried, Germany;

[7]Genomics Core Facility, Imagine Institute and Structure Fédérative de Recherche Necker, INSERM UMR1163 and INSERM US24/CNRS UMS3633, Paris Descartes-Sorbonne Paris Cité University, 75015 Paris, France;

[8]Cell Imaging Platform UMS 24, Structure Fédérative de Recherche Necker, Inserm US24/CNRS UMS3633, 75015 Paris, France;

[9]Bioinformatics Core Facility, Paris Descartes-Sorbonne Paris Cité University, 75015 Paris,

France ;

[10]The Prenatal Diagnosis and Medical Genetics Program, Department of Obstetrics and Gynecology, Mount Sinai Hospital, University of Toronto, Toronto, ON, Canada;

[11]Division of Clinical and Metabolic Genetics, Department of Pediatrics, The Hospital for Sick Children, University of Toronto, Toronto, ON, Canada;

[12]Department of Pathology and laboratory Medicine, Mount Sinai Hospital, University of Toronto, Toronto, ON, Canada;

[13]Department of Medical Genetics, Kasturba Medical College, Manipal, Manipal Academy of Higher Education, Manipal, India;

[14]AP-HP, Louis Mourier Hospital, 92701 Colombes, France

* To whom correspondence should be addressed:

Marion Delous, Laboratory of Inherited Kidney Diseases, Imagine Institute, 24 boulevard du Montparnasse, 75015 PARIS, France. Tel: +33 1 42 75 43 46, Fax: +33 1 42 75 42 25, email: marion.delous@inserm.fr

ABSTRACT

Mutations in genes encoding components of the intraflagellar transport IFT complexes have previously been associated with a spectrum of diseases collectively termed ciliopathies. Ciliopathies relate to defects in the formation or function of the cilium, a sensory or motile organelle present on the surface of most cell types. IFT52 is a key component of the IFT-B complex and ensures the interaction of the two subcomplexes IFT-B1 and IFT-B2. Here, we report novel *IFT52* biallelic mutations in cases with a short-rib thoracic dysplasia (SRTD) or a congenital anomaly of kidney and urinary tract (CAKUT). Combining *in vitro* and *in vivo* studies in zebrafish, we showed that SRTD-associated missense mutation impairs IFT-B complex assembly and IFT-B2 ciliary localization, resulting in decreased cilia length. In comparison, CAKUT-associated missense mutation has a mild pathogenicity, thus explaining the lack of skeletal defects in CAKUT case. In parallel, we demonstrated that the previously reported homozygous nonsense *IFT52* mutation associated with Sensenbrenner syndrome (Girisha et al, 2016) leads to exon skipping and results in a partially functional protein. Finally, our work uncovered a novel role for IFT52 in microtubule network regulation. We showed that IFT52 interacts and partially co-localised with centrin at the distal end of centrioles, where it is involved in its recruitment and/or maintenance. Alteration of this function likely contributes to centriole splitting observed in *Ift52*$^{-/-}$ cells.

Altogether, our findings allow a better comprehensive genotype-phenotype correlation amongst IFT52-related cases and revealed a novel, extra-ciliary role for IFT52 which disruption may contribute to pathophysiological mechanisms.

INTRODUCTION

The primary cilium is a microtubule-based, antenna-like structure which acts as a sensory organelle receiving, integrating and transmitting various external cues (i.e. flow, Hedgehog, Wnt, FGFR, TGFβ) essential for tissue development and homeostasis. The primary cilium is docked at the cell surface from the basal body, a modified centriole. Intraflagellar transport (IFT) is required for the movement of ciliary proteins along axonemal microtubules and is essential for both ciliary formation and function. The IFT-B complex ensures the loading of ciliary proteins at the base of the cilium and their anterograde transport towards tip of the cilium (1). Retrograde transport of ciliary molecules, including IFT-B subunits, back towards the cytoplasmic compartment require the IFT-A complex, which also participates in the fine regulation of ciliary signaling pathways. The IFT-B complex is composed of two subcomplexes, the IFT-B1 core and the peripheral IFT-B2 (2-4). The association of IFT-B1 and IFT-B2 subcomplexes is required for the IFT-B complex to function. The interaction of the IFT52/IFT88 components of IFT-B1 with the IFT38/IFT57 subunits of IFT-B2 ensures this association and occurs via the N-terminal "GIFT" (GldG, intraflagellar transport (IFT)) (5) domain of the IFT52 protein (4).

Mutations in genes encoding ciliary proteins define a wide class of genetic diseases, mostly autosomal recessive, called ciliopathies. These diseases are multisystemic with the most frequently affected organs being the kidneys (renal cystic dysplasia or nephronophthisis), brain (cerebellar vermis aplasia or hypoplasia), liver (fibrosis), skeleton (cranio-ectodermal dysplasia, polydactyly, short ribs, narrow chest) and eyes (retinitis pigmentosa) (6). More particularly, mutations in genes encoding components of IFT-A and IFT-B complexes often lead to skeletal dysplasia, including the short-rib thoracic dysplasia (SRTD; narrow thorax and chest, short ribs, short limbs, with or without polydactyly) or Sensenbrenner syndrome (SRTD signs with cranio-ectodermal dysplasia (craniosynostosis, dental abnormalities, spare

hair)) (7). Nevertheless, other pathologies have been associated to IFT-A/IFT-B mutations, such as Bardet-Biedl syndrome, isolated retinal dystrophy and nephronophthisis-related disorders (8-14). Such phenotypic variability could be explained by the nature of the mutations; however, no clear genotype-phenotype correlations have been established. For instance, mutations in *IFT52* have been previously reported in cases with embryonic lethal SRTD or Sensenbrenner syndrome associated with retinopathy (15-17). While one would expect the SRTD cases to be associated with the most severe mutations, one of the living children presenting a Sensenbrenner syndrome and pigmentary retinopathy carries a homozygous nonsense mutation that supposedly results in a truncated IFT52 protein lacking all functional domains of the protein (16). The second case with Sensenbrenner syndrome is less surprising as it is associated with a homozygous missense mutation, which was reported to alter IFT52 protein stability (17). As for SRTD cases, they are compound heterozygous mutations that combine frameshift and missense mutations (15).

Here, we report three novel human *IFT52* mutations, all located in the GIFT domain of the protein, in two families with distinct lethal phenotypes: SRTD or multicystic dysplastic kidneys, a phenotype belonging to the Congenital Anomalies of the Kidney and Urinary Tract (CAKUT) spectrum. As no kidney defects have been reported to date in individuals harbouring *IFT52* mutations, we sought to analyse the effect of the mutations identified herein on the protein function and ciliogenesis, and showed the mild pathogenicity of the variant associated to CAKUT case compared to those of SRTD cases. In addition, using patient fibroblasts, we studied the previously reported nonsense mutation (16), which we demonstrated to result in a partially functional protein, thus explaining its association with a non-lethal syndrome. Finally, analysis of the *IFT52* mutations has uncovered a new, extra-ciliary role of IFT52 in microtubule anchorage and dynamics, likely contributing to centrosome cohesion.

RESULTS

Identification of *IFT52* mutations in foetuses with distinct phenotypes

In order to identify new genes/mutations involved in SRTD, targeted exome sequencing (ciliome (18, 19)) was performed on 140 individuals from 116 families. This work led to the identification of two variations in the *IFT52* gene (GenBank: NM_016004.2) in a family (F1) presenting two out of three foetuses, F1:II-1 and F1:II-3, that suffered from SRTD signs (polydactyly, short ribs and narrow chest), associated with tortuous ureters and left pelviectasis for foetus F1:II-1 (Table 1, Figure 1A, C1-C2). The identified compound heterozygous variations corresponded to a maternally-inherited variant (c.293A>G) leading to an amino acid change (p.Asn98Ser, hereafter N98S) and a paternally-inherited "indel" mutation, consisting of the deletion of the last five base pairs and the insertion of two base pairs within exon 8 (c.695_699delinsCA), predicted to result in an in-frame mutation (p.Ile232Met233delinsThr, hereafter IMdelT) (Table 1, Figure 1B). Given that this latter mutation affected the last nucleotides of exon 8, we analysed the possible impact of this sequence change on exon splicing. Using a minigene approach, we showed that exon 8 was much less efficiently spliced when harbouring the identified "indel" mutation (F1:II-3 individual) compared to the control (F1:I-1 individual) (Figure 1D). This result indicated that c.695_699delinsCA likely affects the correct splicing of exon 8, thus partially leading to a frameshift mutation. As for the N98S variation (allele frequency 8.297E-06 in gnomAD), it affects an evolutionarily conserved amino acid (Figure 1E) and is predicted to be damaging and deleterious by Polyphen 2, SIFT and CADD (Table S1). This case, therefore, resembles that published by Zhang et al. (15) associating a truncating mutation with a pathogenic missense mutation.

Through an independent whole exome sequencing (WES) study performed on 48 individuals with CAKUT from 26 families, we identified a homozygous variation (c.775G>C)

in *IFT52* in a female foetus (F2:II-3) from a North African consanguineous family (F2, Figure 1A). This affected foetus presented with bilateral isolated multicystic kidney dysplasia characterized by enlarged kidneys (3 to 4 times the expected size compare to age-matched control kidney (weight of F2:II-3 kidney was 14g *vs* <4g at 20 weeks in average in controls) with voluminous cysts distributed in a disorderly way and without differentiated nephron structure (Figure 1C3-C4), which led to medical termination of the pregnancy (Table 1). No skeletal defect was reported in this foetus (Figure 1C5). Two neonatal deaths due to unknown causes were additionally observed in this family (Figure 1A). The c.775G>C variation (allele frequency 0.0004081 in gnomAD, with an enrichment in Latino population (0.001757)) is present in a heterozygous state in both parents and results in the change of a conserved amino acid, p.Asp259His (hereafter D259H). It is predicted to be damaging and deleterious by Polyphen 2, SIFT and CADD even though an individual homozygous for this variant has been reported in gnomAD (Figure 1B, E, Table S1). Given the genetic information on this variant and the clinical traits associated with the *IFT52* mutations reported so far (Table 1) (15-17), we assumed that it was not as pathogenic as N98S for bone development, but nevertheless, could have a specific effect on kidney development and thus could contribute to cystic kidney dysplasia.

In addition, we found surprising the phenotype of the previously reported individual harbouring a homozygous nonsense mutation in *IFT52* (c.424C>T, p.Arg142*, hereafter p.R142*). This 3-year-old child presented a Sensenbrenner syndrome and pigmentary retinopathy (Table 1) (16). Since the c.424C>T mutation was predicted to affect a putative exonic splicing enhancer in exon 6, we hypothesized that it could induce skipping of this in-frame exon. RT-PCR analysis from patient and age-matched control fibroblasts showed that the mutation c.424C>T indeed resulted in a partial skipping of exon 6 (Figure 1F). Western blot analysis further confirmed the expression of a shorter protein corresponding to the

deletion of the 24 amino acids of this exon (hereafter, Δex6) (Figure 1G). It is noteworthy that the Δex6 IFT52 protein was expressed to a much lower degree than the wild type (~10%) (Figure 1G, H) while the expected truncated protein resulting from the p.R142* mutation could not be detected by Western blot. This result indicated that either both transcripts - full-length with nonsense mutation and that with skipped exon 6 - underwent nonsense-mediated RNA decay, or the mutated proteins were unstable. Altogether, these data demonstrated that c.424C>T rather leads to a partially functioning protein than a total loss of IFT52 function. This observation can explain the milder phenotype of Sensenbrenner syndrome.

Remarkably, most of the mutations reported in *IFT52*, including the one reported here, are located in the N-terminal GIFT domain of the protein (Figure 1I, J) (15-17), which suggests a crucial role of this domain in the function of IFT52. Moreover, to better understand the genotype-phenotype correlation of mutations associated to this domain, we sought to compare the impact of N98S, D259H and Δex6 on the protein function to evaluate their pathogenicity and the potential contribution of D259H to the CAKUT phenotype.

Missense *IFT52* mutations do not restore WT phenotype in *ift52*$^{-/-}$ zebrafish embryos

To evaluate the pathogenicity of the N98S and D259H missense variations, we first used the zebrafish model, an organism well-suited to *in vivo* study of ciliary functions (20). As observed in various *ift* mutant lines, ciliary dysfunction in the zebrafish leads to a set of ciliopathy-related phenotypes, notably body axis curvature, pronephric cysts, *situs inversus*, retinal degeneration and otolith defects (21-23).

As expected, CRISPR/Cas9-mediated mutation of *ift52* in the zebrafish (Figure S1A; hereafter *ift52*$^{-/-}$) induced ciliopathy-related phenotypes, i.e. ventral body curvature and kidney cysts at 48 hours post fertilization (hpf) (Figure 2A-D), in ¼ of the embryos from crosses of heterozygous (het) individuals (Figure S1B). These phenotypes were fully

penetrant and heterozygous embryos were indistinguishable from WT siblings. In accordance with the known function of Ift52 in ciliogenesis, the *ift52*$^{-/-}$ embryos lacked cilia in multiciliated organs at 72hpf, including the olfactive placode (Figure 2E, F) and the proximal tubules of the pronephros (Figure 2G-H). These phenotypes were concordant with those observed in *ift52* morpholino-injected embryos (22). In addition, *ift52*$^{-/-}$ larvae exhibited morphometric alterations of the lower jaw at 4dpf, with a reduced distance between Meckel's cartilage and the hyoid arches (Figure S1C, D). As in mammals (24), Hedgehog (Hh) signalling pathway is required for craniofacial cartilage development in zebrafish (25), and its regulation also depends on cilia (26). By qRT-PCR analysis, we studied the expression of Hh target genes*, ptc1, ptc2* and *gli1,* and showed that *ptc2* and *gli1* were decreased in mutant heads compare to WT/het samples (Figure S1E), thus confirming the involvement of Ift52 in Hedgehog signaling regulation (27). We subsequently performed rescue experiments by injecting zebrafish WT and mutated *ift52* RNA into *ift52*$^{-/-}$ embryos. In contrast to *ift52*$^{-/-}$ embryos injected with WT *ift52* RNA, those injected with D259H and N98S RNA exhibited body curvature (87.8% and 79.31%, respectively) and pronephric cysts (90.24% and 75.86%, respectively) (Figure 2I, J), indicating that the two missense mutations were pathogenic *in vivo*.

Missense mutations differentially affect ciliogenesis and IFT-B subunit interactions.

To further characterise the impact of the missense variations and Δex6 on protein function, a CRISPR/Cas9-mediated *Ift52* knock-out cell line (hereafter, *Ift52*$^{-/-}$) was generated in murine Inner Medullar Collecting Duct cells (IMCD3) (Figure S2A), in which stable expression of murine GFP-tagged WT-, D259H-, N98S-, and Δex6-IFT52 proteins or GFP alone (control) was performed by lentiviral infection (Figure S2B). As expected, the loss of Ift52 led to an absence of primary cilia in these cells, which was fully rescued by expression of WT-Ift52

protein (Figure 3A, B). Expression of the D259H- and N98S-mutant forms also restored the percentage of ciliated cells; however, they resulted in shorter cilia, N98S mutation being associated to a higher proportion of short cilia (26.9% *vs* 14% of cilia <1µm) (Figure 3A-C). On the contrary, expression of the Δex6-Ift52 form resulted in a decreased percentage of ciliated cells and very short cilia (53% <1µm) (Figure 3A-C). Similar ciliary defects were also observed in patient fibroblasts (Figure 3D-F).

Then, as the mutations are located in the N-terminal GIFT domain, we investigated their effects on the binding with other IFT-B subunits. The side chain of Asn98 makes two H-bonds with main-chain of Phe65 that are likely disrupted by the amino acid change to Ser. As a comparison, we also analysed p.Ile232Met233delinsThr mutation that, if expressed, alters the hydrophobic cores of the GIFT domain possibly resulting in mis-folding of the domain (Figure 4A). Pull down of GST-tagged 1-335 constructs of *C.reinhardtii* IFT52 showed that mutant forms were hardly soluble compare to WT (Figure S2C), suggesting a mis-folding or instability of the mutant proteins. Co-expression of a sumoylated IFT88 fragment (118-437) could stabilize the N98S form but not IMdelT, indicating that this latter mutant form was severely mis-folded (Figure S2D). This result was further confirmed by size exclusion chromatography showing that IMdelT peptides formed aggregates whereas the N98S mutant was soluble but resulted in lower purification yield than WT protein (Figure S2E)**.** As for D259H mutation, it did not seem to alter GST-tagged construct expression neither interactions with other IFT-B subunits in *E.coli* (data not shown). Then, we performed mass spectrometry analysis on GFP immunoprecipitates from GFP-WT, -D259H, -N98S and GFP alone (control) expressing *Ift52*$^{-/-}$ cells. Most IFT-B subunits (except Ift54, Ift20 and Ift25) were identified in GFP-Ift52 immunoprecipitates (Figure 4B-D). Interactions with the IFT-B subunits appeared slightly affected by the D259H mutation with notably the loss of IFT46 binding (Figure 4B, C). In contrast, half of the IFT-B proteins identified in the WT condition became non-

significantly bound with the N98S mutant (grey filled circles, Figure 4D). Of note, the chaperone protein Bag2 was identified as a putative partner of N98S-Ift52 protein, further suggesting a mis-folding of this mutant form. To confirm these results, we performed co-immunoprecipitation assays and analysed the interaction of Ift52 with its direct partners, Ift38 and Ift57 (in green in Figure 4B-D). Both missense mutations diminished the interaction of Ift52 with endogenous Ift38 and Ift57 proteins, with a higher effect of the N98S mutation compared to D259H (Figure 4E, F). As for Δex6 mutant form, we observed that it totally abrogated the interactions of Ift52 with both Ift38 and Ift57 (Figure 4E, F), which is coherent with the deletion of 24aa within the GIFT domain.

To assess whether the mutations affected IFT-B ciliary localisation, we performed immunostainings and observed that contrary to WT and D259H, relatively small amounts of the N98S-Ift52 mutant form entered the cilium (Figure 4G, H). As a consequence, localisation of Ift38 and Ift57 along the axoneme decreased in N98S-Ift52 expressing cells, whereas it was maintained in presence of D259H-Ift52 protein (Figure 4I, J). As for Δex6 mutant form, we observed that, like D259H, it succeeded to localise along the ciliary axoneme and that despite the total loss of interaction, its partners Ift38 and Ift57 managed too (Figure 4G-J). This observation may be explained by the fact that IFT38/57, in addition to its interaction with IFT52, also interacts directly with IFT20/54, IFT80 and IFT172 (4).

Altogether, these data indicated that all tested mutations were pathogenic with differential effects on the interaction with IFT-B2 subunits and their ciliary localisation. Notably, D259H mutation proved to have a milder effect on the protein function than the N98S mutation, which explained the lack of skeletal defects in foetus with CAKUT. However, our demonstration that the D259H variant was unable to rescue pronephric cysts in *ift52*$^{-/-}$ zebrafish embryos suggested that it could play a role in the mechanism leading to cystic kidney dysplasia.

Ift52 interacts and partially colocalizes with centrin

As we observed that Ift52 localises to the two centrioles in non-ciliated cells, even during mitosis (Figure S2F-G), and that proteomic data revealed centrin and γ-tubulin as putative interaction partners of Ift52 (Table 2), we investigated whether Ift52 could have a role at the centrosome. For this, we first investigated the precise localisation of Ift52 at the centrosome and performed immunostainings of GFP-Ift52 with c-Nap1, a proximal marker of centrioles, and with centrin and γ-tubulin, which decorate the distal and proximal sides of centrioles, respectively. We observed that GFP-Ift52 localization did not overlap with that of c-Nap1 or γ-tubulin; however, it partially co-localised with centrin at the distal side of the mother centriole (Figure 5A, B). To strengthen the link between Ift52 and centrin, we performed co-immunoprecipitation assays by co-expressing tagged versions of both proteins in HEK293T cells and showed that WT GFP-Ift52 protein interacted with centrin-mCherry, while D259H and N98S tended to alter this interaction either by reinforcing or weakening it (Figure 5C, D), suggesting that the role of Ift52 with centrin at the centrosome could participate in the physiopathological mechanisms. Finally, we analysed the localisation of centrin and observed that centrin staining appeared weaker at the centrioles and more dispersed around the centrosome in *Ift52*$^{-/-}$ cells than in control cells (Figure 5E, F). On the other hand, exogenous expression of WT GFP-Ift52 seemed to help concentrating centrin to the centrosome. Altogether, these results indicated that Ift52 would contribute to the recruitment and/or maintenance of centrin at the centrosome.

***Ift52*$^{-/-}$ cells display defective microtubule anchorage and dynamics**

Centrin is a known regulator of centriole elongation (28) and its loss of function leads to altered microtubule anchoring at the centrosome associated with disorganised microtubule network (29). Thus, we sought to investigate the role of IFT52 in microtubule anchorage and

dynamics. First, we performed a microtubule regrowth assay, by treating cells with nocodazole (50µM) for 1 hour (T0) and followed microtubule nucleation at the centrosome (T+5min) and growth (T+10min) after drug removal. At T+5min, microtubule properly nucleated at both centrioles in *Ift52*$^{-/-}$ cells (Figure 6A); however, they failed to grow and form asters as large as that of control and WT-expressing cells, which persisted at T+10min (Figure 6A, B). Of note, we observed unanchored and dispersed microtubules in *Ift52*$^{-/-}$ cells (Figure 6A, arrows), suggesting a defect in microtubule anchorage at the centrosome. To further evaluate microtubule growth defects, we performed immunostainings of EB1, a plus-end microtubule associated protein involved in microtubule dynamics. We observed that EB1-positive comets were shorter in *Ift52*$^{-/-}$ cells compared to Ctrl and WT-expressing *Ift52*$^{-/-}$ cells, indicating that microtubules were indeed less dynamic (Figure 6C, D). Finally, additional hints came from the low dose nocodazole (100nM) treatment, which blocks the dynamic instability of microtubules and results in an increased microtubule lifetime and acetylation (30, 31). Such treatment triggered a hyperacetylation of cytoplasmic microtubules in *Ift52*$^{-/-}$ cells only (Figure 6E), suggesting that these cells were more sensitive to low dose nocodazole, and that alternation of growth and shrinkage phases occurred at a slower rate, overall decreasing microtubule extension. Similarly, cytoplasmic microtubule hyperacetylation was observed in multiciliated pronephric cells of *ift52* mutant zebrafish embryos (Figure 6F). Altogether, these results indicated that microtubule anchorage to centrosome as well as dynamics were impaired in *Ift52*$^{-/-}$ cells.

Ift52$^{-/-}$ cells exhibit centriole splitting

During our investigations, we noticed that *Ift52*$^{-/-}$ cells showed abnormal distance between the centrioles of the centrosome (Figure 3A, 7A). This phenotype was not concomitant with entry in M phase, as split centrosomes were not duplicated centrosomes and cells were Ki67^{-} (Figure S3A, B). Moreover, distance between centrioles was fully rescued by the expression

of WT-Ift52 but not by D259H- or N98S-mutated forms (Figure 7A), suggesting that Ift52 contributed to centrosome cohesion in quiescent cells. Centrosome cohesion is mostly guaranteed by the protein linker that physically links the proximal regions of the centrioles by thin filaments. One of its major components is c-Nap1 (alias CEP250) (32), which serves as anchoring points for rootletin, Cep68 and LRCC45 that form the thin filaments of the linker (33, 34). Loss of function of each of these proteins leads to premature centriole splitting (32-35). However, we showed that Ift52 did not colocalized with c-Nap1 (Figure 5B) and immunostainings of c-Nap1, rootletin, Cep68 and LRCC45 did not reveal any obvious defects of localisation of these proteins to the centrosome in *Ift52*$^{-/-}$ cells compared to control cells (Figure S3C-E).

The second element that participates to centrosome cohesion is the microtubule network, which exerts forces onto the centrosome, maintaining the centrioles in close proximity in the absence of the protein linker (36-38). To confirm this hypothesis, we tested whether a destabilisation of the protein linker would reveal the microtubule defects as performed in (38). For this, we treated cells with a low dose of siRNA targeting c-Nap1 that had no effect in control and WT-expressing cells but which increased centriole splitting in *Ift52*$^{-/-}$ cells (3.75µm in average in c-Nap1 siRNA treated *Ift52*$^{-/-}$ cells *versus* 2.21µm in luciferase siRNA treated cells) (Figure 7B, C). This result suggested that alteration of microtubule anchorage and dynamics weakened microtubule forces applied onto the centrioles, thus contributing to centriole splitting observed in *Ift52*$^{-/-}$ cells, even though we cannot exclude that another structural centriolar defect may intervene.

Altogether, our data indicate that Ift52 has a dual function: it is required for ciliogenesis as well as at the centrosome to maintain centrin at the distal end and regulate microtubule anchorage and dynamics, thus ensuring centrosome cohesion.

DISCUSSION

We report here a family with SRTD associated to *IFT52* by identifying novel compound heterozygous mutations: a missense variation (p.N98S) combined to a frameshift mutation. Our *in vivo* and *in vitro* studies confirmed the pathogenicity of the missense mutation p.N98S, which altered the conformation and/or stability of the protein, and consequently the assembly of the whole IFT-B complex. The mutation decreased the interaction of IFT52 with the peripheral subunits IFT38 and IFT57 and impaired the localization of IFT52 and its direct partners into the cilium. These alterations likely explain the ciliogenesis defects we observed in IMCD3 cells, and could lead to Hedgehog signaling misregulation and subsequent skeletal anomalies *in vivo*. This case confirms that previously reported (15).

We also studied a foetus with bilateral multicystic dysplastic kidneys where we identified a missense homozygous mutation in *IFT52* (p.D259H). This mutation is pathogenic as shown in rescue experiments in zebrafish; however, its effects clearly appeared less severe than the SRTD-related missense mutation in our *in vitro* experiments. Even though the D259H mutation diminished the interaction of IFT52 with IFT38 and IFT57, it did not destabilize the whole IFT-B complex and preserved the localization of IFT52 and its partners into the cilium, suggesting that it could ensure sufficient ciliary signaling. Even though the milder pathogenicity of p.D259H can explain the absence of skeletal defects in the affected foetus, it cannot be excluded that this variant would contribute to post-natal bone development anomalies as observed for *IFT172* mutations in patients with Saldino-Mainzer syndromes (39). Moreover, we hypothesize that this variant can participate to the development of multicystic dysplastic kidneys, likely in interaction with other variants in (an)other gene(s). Examples of oligogenism or gene modifiers have been reported in ciliopathies (40-42) and the concept of mutational load is well admitted (43). In addition to the *IFT52* homozygous variant, WES of F2:II-3 proband allowed the identification of

homozygous missense variants in two other protein encoding genes, *WNK4* (c.2023C>T; p.R675W, 0.00004604 in gnomAD) and *UBE2C* (c.374A>G; p.D116G, absent from public databases). Both variations are rare and predicted to be damaging by Polyphen 2, SIFT and CADD (Table S2). *WNK4* encodes a serine-threonine kinase expressed in the distal nephron and involved in electrolyte homeostasis in mature kidneys. Heterozygous missense mutations of *WNK4* are associated with pseudohypoaldosteronism type II (hypertension, increased renal salt reabsorption, impaired K^+ and H^+ excretion), which makes *WNK4* an improbable candidate (44). *UBE2C* encodes an ubiquitin-conjugating enzyme implicated in metaphase/anaphase transition (45). UBE2C has recently been shown to be one of the top markers, along with TOP2A and CENPF, of the proliferating cells in the human developing kidney (46). Further investigations will be necessary to determine the causative mechanism leading to multicystic dysplastic kidneys and to explore the contribution of IFT52 p.D259H variation in this pathophysiological mechanism.

Considering the essential role of IFT52 in ciliogenesis, it was surprising that a homozygous truncating mutation could be associated with a viable phenotype, i.e. Sensenbrenner syndrome (16). Using patient fibroblasts, we showed that the nonsense mutation led to the in-frame skipping of the exon 6 and resulted in a shorter protein, deleted of 24 amino acids. This mechanism, called nonsense-associated altered splicing (NAS), allows for the bypass of the nonsense mutation. Although the resulting protein lacks 24 amino acids within the GIFT domain that prevents the interaction with IFT38 and IFT57 partners, it might ensure sufficient functions to allow ciliary signalling. Indeed, as for p.D259H, we observed that Δex6-Ift52 protein as well as its partners were able to enter the cilia where they could maintain, to some extent, ciliary signalling. It should be noted that this mutant IFT52 lacking 24 residues in the GIFT domain still has intact domains for the interaction with IFT70 and IFT88, two other IFT-B1 components. We can also speculate that a second mutation inherited with IFT52

p.R142* could act as a protective modifier that compensates the loss of fully functional IFT52. For instance, it was shown that combination of Cep290 and Mkks mutations in mice rescued cilia formation and sensory functions altered in single mutant animals (47). Overall, this case shows the importance of the thorough analysis of the pathogenicity and significance of IFT-B mutations. Such analysis would reveal mechanisms that bypass truncated mutations to favor the synthesis of a partially functional protein and ensure compatibility with life.

During our study, we noticed that loss of function of Ift52 in IMCD3 cells caused centriole splitting. This unexpected phenotype led us to explore the underlying mechanism and discover that Ift52 interacted and partially localized with centrin at the distal end of the centrioles. We also showed that in *Ift52*$^{-/-}$ cells, microtubules failed to anchor at the centrosome, and that they were less dynamic as revealed by shorter EB1-positive comets and their hyperacetylation upon low dose nocodazole treatment. Thus, we concluded that Ift52 is required to recruit/maintain centrin at the centrosome, favoring microtubule anchorage and dynamics that contributes to centrosome cohesion. Nevertheless, we cannot exclude that Ift52 also participates in maintaining other centriolar structures that directly ensure centrosome cohesion.

Finally, we showed that missense mutations (p.N98S and p.D259H) altered the interaction of IFT52 with centrin and were not able to rescue centriole splitting, suggesting that this novel function of IFT52 in microtubule regulation could participate to the pathogenic mechanisms. Extra-ciliary functions of IFT-B proteins have already been demonstrated. For instance, IFT54 is a negative regulator of cytoplasmic microtubule stability that competes with MAP4 or helps for its degradation, to modulate microtubule dynamics (9). Loss of IFT54 function was associated with abnormal stability of cytoplasmic microtubules in patient fibroblasts and kidneys. IFT88 has been shown to participate to the formation of mitotic astral microtubule arrays, favoring the proper planar orientation of the mitotic spindle axis (48).

Alteration of such orientation of cell division along the developing renal tubule axis was suggested to contribute to cystogenesis in kidney (49). Interestingly, IFT52 was shown to interact with IFT88 at the mitotic spindle poles (48), so that we can speculate that Ift52 also controls microtubule dynamics during mitosis. Even though we showed that p.D259H IFT52 is unlikely to cause multicystic dysplastic kidneys on its own, we can imagine that the alteration of IFT52 function in microtubule anchoring and polymerization can contribute to cyst formation.

Taken together, our data allowed to have a better comprehensive overview of the genotype/phenotype correlation associated to *IFT52* mutations, and shed light on a novel function of IFT52 on centriole cohesion via the regulation of microtubule anchorage and dynamics.

MATERIAL AND METHODS

Ethics statement

This study was conducted with the approval of the «Comité de Protection des Personnes pour la Recherche Biomédicale - Ile de France II». Approval was obtained under numbers 2007-02-09/DC-2008-229 and 2009-164/DC-2011-1449 (CAKUT cases). For each case, written informed consent was obtained from the parents.

Patients

48 cases with Congenital Anomalies of Kidney and Urinary Tract (CAKUT) from 26 families and 140 foetuses or patients with short rib-polydactyly syndrome or Jeune asphyxiating thoracic dysplasia were studied. Genomic DNA was isolated from peripheral blood or frozen tissues using standard procedures. Kidney sections from an age-matched control and F2:II-3 proband were stained by hematoxylin-eosin (HE) and HE-saffron, respectively.

Mutation screening using WES or "Ciliome" sequencing

Whole exome sequencing was performed using the 50Mb Agilent SureSelect all exon V3. Ciliary exome-targeted sequencing was conducted using a custom SureSelect capture kit (Agilent Technologies) targeting 4.5Mb of 20,168 exons (1 221 ciliary candidate genes), including IFT52 (18, 50). Sequencing was performed on a HiSeq2500 (Illumina) sequencer. Sequence data were aligned to the human genome reference sequence (hg19 build) using BWA aligner. Downstream processing was carried out with the Genome Analysis Toolkit (GATK), SAMtools, and Picard (http://www.broadinstitute.org/gatk/guide/topic?name=best-practices). Variants were annotated using a software system developed by the Paris Descartes University Bioinformatics Platform, based on the Ensembl (GRCh37/hg19), dbSNP, EVS,

1000 genome, ExAC and GnomAD databases. Variants were then prioritized according to their damaging effect (nonsense, frameshift, acceptor/donor splice site mutations, missense variants predicted to be damaging), and their low frequency in GnomAD and in our in-house database (> 10 000 exomes). For missense variants, prediction of damaging effect was based on PolyPhen2, SIFT and CADD scores.

Plasmids and mutagenesis

pLVTH-His-GFP-Ift52 was a gift from Esben Lorentzen (51). The missense mutations were obtained by site-directed mutagenesis using Pfu Turbo kit (Invitrogen) and deletion of the exon 6 was created using Q5 site-directed mutagenesis kit (New England Biolabs). pIRES-Centrin1-mCherry was a gift from Matthieu Piel (Addgene plasmid #64340).

For zebrafish rescue experiments, full length zebrafish *ift52* coding sequence was amplified by RT-PCR from total 24hpf cDNA and cloned into pCS2 plasmid according to the Cold Fusion kit protocol (SBI System Biosciences), using the following primers: z*ift52*-pCS2_F: 5'- acgactcactatagttctagAGCTCCACTGCAGATTGAGT-3' and z*ift52*-pCS2_R: 5'-gctacttgttctttttgcagCGCATTATAACTCCCCACAGC-3'.

Cell culture, establishment of *Ift52*$^{-/-}$ mIMCD3 cell lines and transfection

Human primary fibroblasts were derived from skin biopsy of Family 3 patient (F3-Pt) and cultured into OptiMEM medium, supplemented with 10% fetal bovine serum, glutamine and penicillin/streptomycin (Invitrogen) up to 11 passages. Control and patient fibroblasts were plated on coverslips and ciliogenesis was induced by 24 hours of serum starvation when cells reached confluence. HEK293T were cultured in Dulbecco's Modified Eagle Medium (DMEM) and murine Inner Medullary Collecting Duct (IMCD3) cells in DMEM F-12, both supplemented with 10% fetal bovine serum, glutamine and penicillin/streptomycin

(Invitrogen). mIMCD3 cells were plated on coverslips and grown for 2 days post-confluence in absence of serum to induce ciliogenesis.

Guide RNA sequence targeting exon 3 of murine Ift52 (5'-GTGAAACTATGGATCACAGC*TGG*-3') was designed using CRISPOR online tool (http://crispor.tefor.net) (52) and cloned into pSpCas9(BB)-2A-GFP (pX458) (gift from Feng Zhang, Addgene plasmid #48138) following the protocol described in (53). mIMCD3 cells were transfected using Lipofectamine 2000 (Invitrogen) and GFP-positive cells were sorted using flow cytometry. Clonal populations were obtained after serial dilution (protocol from "Cell cloning by serial dilution in 96 well plates", Corning, John A. Ryan) and their genotype was established by Sanger sequencing of genomic DNA using following primers: mIft52_F: 5'-GAACCTAGCCTGGATGCCTC-3' and mIft52_R: 5'-CAGTGGGCTTACTCTGTGGG-3'. Stable reexpression of WT and mutated GFP-Ift52 forms into *Ift52*$^{-/-}$ mIMCD3 cells was performed by lentiviral infection and infected cells were sorted according to the GFP level by flow cytometry.

For siRNA transfection, 0.5µM of siRNA targeting murine c-Nap1 (ON-TARGETplus, J0464666-05-0010; Dharmacon) or luciferase (5' - GCCATTCTATCCTCTAGAGGATG - 3') were transfected into mIMCD3 cells using Lipofectamine RNAiMAX (Invitrogen). Media was changed 12 hours after transfection, and cells were harvested for 3 days prior to immunostaining or RNA extraction. For plasmid transfection, 5µg of GFP-Ift52 and centrin1-mCherry were co-transfected into HEK293T cells using Lipofectamine 2000 (Invitrogen) according to the protocol's manufacturer.

Minigene assay

Sequences of human *IFT52* exon8, flanked by 150-200bp of adjacent introns, were amplified from the genomic DNA of mother F1:I-1 (control) and the foetus F1:II-3 (carrying c.695-

699delinsCA) and cloned into pSpliceExpress vector (54) (gift from Stefan Stamm, Addgene plasmid #32485) using Gateway cloning system. Briefly, two rounds of PCR were used to add attB1/attB2 (in bold below) homology arms to IFT52 sequences (first round with attB1/IFT52_F: 5'-**AAAAAGCAGGCT**TGGGTGTGAATTGGCACTCT-3' and attB2/IFT52_R: 5'-**AGAAAGCTGGGT**CCCCACCTGACATGCTCAG-3', and second round with attB1adapter_F: 5'-GGGGACAAGTTTGTACA**AAAAAGCAGGCT**-3' and attB2adapter_R: 5'-GGGGACCACTTTGTACA**AGAAAGCTGGGT**-3'). PCR products were then cloned using BP Clonase II enzyme (Gateway® BPClonase®II Enzyme mix, Invitrogen). Two micrograms of each construction were transfected into HEK293T cells using FuGene (Promega) and RNA was extracted 48 hours after.

RNA extraction, RT-PCR and qRT-PCR

Total cellular or zebrafish mRNA was isolated from cell lysates and treated with DNaseI using Qiagen Extraction Kit. Five micrograms of total RNA were reverse-transcribed using SuperscriptII (Invitrogen) following instructor's guidelines. For minigene approach, RT-PCR was performed using the following primers: INSratEx2_F: 5'-TCGATCCGCTTCCTGCCCC-3' and INSratEx3_R: 5'-CACCTCCAGTGCCAAGGTC-3'. For testing IFT52 exon6 skipping, following primers were used: hIFT52-ex5_F: 5'-TTCCATCCTAAAGAAGCTCT-3' and hIFT52-ex7_R: 5'-TTGAGTGATAGAAAGCCAAA-3'. Housekeeping gene was used as control: hHPRT_F: 5'-TCTTTGCTGACCTGCTGGATT-3' and hHPRT_R: 5'-GTTGAGAGATCATCTCCACCAATTACT-3'.

Relative mRNA expression of zebrafish Hedgehog target genes was assessed by qRT-PCR using the following primers: zptc1_F: 5'-CTTCGCTGTTTTGGCCATCC-3' and zptc1_R: 5'-GGAGATACCTCAGGATAAGGGC-3'; zptc2_F: 5'-GCACATTGCACTGGGTTTCC-3'

and zptc2_R: 5'-TGTTCCATAGCAACGGCTGA-3'; zgli1_F: 5'-TCAGGAGACGCCTCTTGTTT-3' and zgli1_R: 5'-AGAGCGCGCTTCTTACTGAG-3'. mRNA expression was normalized to that of gapdh (zgapdh_F: 5'-GTTGGTATTAACGGATTCGGTC-3' and zgapdh_R: 5'-CACTTAATGTTGGCTGGGTC -3') and comparative Ct quantification method was applied.

Antibodies

The following antibodies were used in this study: IFT52 (17534-1-AP, 1:50 (IF), 1:1000 (WB)), IFT57 (11083-1-AP, 1:200 (IF), 1:1000 (WB)), IFT38 (17470-1-AP, 1:200 (IF), 1:1000 (WB)), Arl13b (17711-1-AP, 1:200 (IF)) from ProteinTech; Ki67 (ab16667, 1:400 (IF)), α-tubulin (ab18251, 1:500 (IF)) from Abcam; γ-tubulin (sc-7396, 1:200 (IF)) from Santa Cruz; acetylated α-tubulin (clone 6-11B-1, 1:10000 (IF)), α-tubulin (clone B-5-1-2, 1:1000 (WB)), phalloidin-TRITC (P1951, 1:300), LRRC45 (HPA024768, 1:200 (IF)) from Sigma-Aldrich; dsRed (632496, 1:1000 (WB)) from TaKaRa; EB1 (610534, 1:300 (IF)) from BD Biosciences; centrin (clone 20H5, 1:400 (IF), 1:1000 (WB)), GAPDH (clone 6C5, 1:1000 (WB)), chicken anti-GFP (AB16901, 1:200 (IF in zebrafish)) from Millipore; rabbit anti-GFP (A11122, 1:1000 (WB), 1:200 (IF in cells)) from Invitrogen; mouse anti-GFP (11814460001, 1:200 (IF in cells), 1:1000 (WB)) from Roche. c-Nap1 (1:200 (IF)), cep68 (1:200 (IF)) and Rootletin (1:200 (IF)) antibodies were kindly given by E. Niggs. Highly cross adsorbed secondary antibodies (Alexa Fluor 488, 555 and 647) were obtained from Molecular Probes (Life Technologies) and were used at 1:200.

Immunostaining and image analysis

mIMCD3 and fibroblast cells were fixed in methanol at room temperature or at -20°C for microtubule staining. After 1 hour blocking in PBS; BSA1%; Tween 0.1%, cells were

incubated with appropriate primary antibodies overnight at 4°C, followed by secondary antibodies for 30 minutes at room temperature. All antibodies were diluted in blocking buffer (see Antibodies section for dilution). DNA was stained with Hoechst (1:40000, #33342 Sigma-Aldrich) and coverslips were mounted in Mowiol media.

Zebrafish embryos were fixed in Methanol:DMSO (80:20) and incubated overnight with primary antibodies at 4°C followed by secondary antibodies for 2 hours at room temperature. Samples were analysed under an inverted confocal microscope Zeiss LSM 700 and images were processed with ZEN 2011 and ImageJ softwares and images were mounted on Photoshop.

Co-immunoprecipitation and immunoblotting

Fibroblast, HEK293T and mIMCD3 cells were lysed in 50mM Tris-HCl pH7.5, 150mM NaCl, 0.5% Triton X-100 supplemented with protease inhibitor cocktail (Roche) and treated in accordance with the Miltenyi-Biotec beads protocol. Protein quantification was then performed using the BCA protein assay kit (Thermo Scientific). For input, 30 to 50µg of proteins were loaded on 10% acrylamide gels, blotted on PVDF membrane (Millipore). The membrane was incubated using the indicated antibodies. Western blots were then analyzed with ImageJ software.

Affinity-pulldown experiments

His-GST-tagged CrIFT52$_{1-335}$ protein construct (WT or mutant form) was expressed alone (Figure S2C) or co-expressed with SUMO-tagged IFT88$_{118-437}$ (Figure S2D) as previously described (4). Briefly, 1 mL *E.coli* lysates containing over-expressed IFT52 proteins or IFT52/88 protein complexes were immobilized on 25 µl Ni^{2+}-NTA affinity beads. After incubation for 30 min, the beads were collected (500 g, 4°C) and washed 3X with buffer

containing 50 mM Tris*HCl pH 7.5, 150 mM NaCl, 10% glycerol, 20 mM Imidazole and 5 mM 2-mercaptoethanol before eluting bound protein(s) with buffer containing 500 mM Imidazole. Eluted samples were examined by SDS-PAGE. Complex purified using the his-tag was subjected to size exclusion chromatography (SEC) using a superdex75 column in the buffer 10 mM Hepes pH 7.5, 150 mM NaCl and 1 mM DTT.

NanoLC-MS/MS protein identification and quantification

S-Trap™ micro spin column (Protifi, Hutington, USA) digestion was performed on IP eluates in Leammli buffer according to manufacturer's protocol, using 2 extra washing steps for thorough SDS elimination. Samples were digested with 3µg of trypsin (Promega) at 47°C for 1h. After elution, peptides were finally vacuum dried down and resuspended in 21µL of 10% ACN, 0.1% TFA in HPLC-grade water prior MS analysis. For each run, 5µL were injected in a nanoRSLC-Q Exactive PLUS (RSLC Ultimate 3000) (Thermo Scientific). Peptides were loaded onto a µ-precolumn (Acclaim PepMap 100 C18, cartridge, 300µm i.d.×5 mm, 5µm) (Thermo Scientific), and were separated on a 50cm reversed-phase liquid chromatographic column (0.075mm ID, Acclaim PepMap 100, C18, 2µm) (Thermo Scientific). Chromatography solvents were (A) 0.1% formic acid in water, and (B) 80% acetonitrile, 0.08% formic acid. Peptides were eluted from the column with the following gradient 5% to 40% B (38 minutes), 40% to 80% (1 minute). At 39 minutes, the gradient stayed at 80% for 4 minutes and, at 43 minutes, it returned to 5% to re-equilibrate the column for 16 minutes before the next injection. Two blanks were run between each series to prevent sample carryover. Peptides eluting from the column were analyzed by data dependent MS/MS, using top-10 acquisition method. Peptides were fragmented using higher-energy collisional dissociation (HCD). Briefly, the instrument settings were as follows: resolution was set to 70,000 for MS scans and 17,500 for the data dependent MS/MS scans in order to increase

speed. The MS AGC target was set to 3.10^6 counts with maximum injection time set to 200ms, while MS/MS AGC target was set to 1.10^5 with maximum injection time set to 120ms. The MS scan range was from 400 to 2000 m/z.

Data Processing Following LC-MS/MS acquisition

The MS files were processed with the MaxQuant software version 1.5.8.3 and searched with Andromeda search engine against the database of *Mus musculus* from swissprot 07/2017. To search parent mass and fragment ions, we set an initial mass deviation of 4.5ppm and 20ppm respectively. The minimum peptide length was set to 7 amino acids and strict specificity for trypsin cleavage was required, allowing up to two missed cleavage sites. Carbamidomethylation (Cys) was set as fixed modification, whereas oxidation (Met) and N-term acetylation were set as variable modifications. Match between runs was not allowed. LFQ minimum ratio count was set to 2. The false discovery rates (FDRs) at the protein and peptide level were set to 1%. Scores were calculated in MaxQuant as described previously (55). The reverse and common contaminants hits were removed from MaxQuant output. Proteins were quantified according to the MaxQuant label-free algorithm using LFQ intensities (55, 56).

Five independent immunoprecipitations of GFP-Ift52 WT, N98S, D259H, and the GFP alone were analysed with Perseus software (version 1.6.0.7) freely available at www.perseus-framework.org. The LFQ (Label-free Quantification) data were transformed in log2, and proteins which were never identified in the GFP alone (control) and identified in at least 3 replicates in at least one group are reported in the table as “specific”. All the proteins identified in at least 4 replicates were submitted to statistical test (volcano plot, FDR=0.05 and S0=0.1) after imputation of the missing value by a Gaussian distribution of random

numbers with a standard deviation of 20% relative to the standard deviation of the measured values and 2.5 standard deviation downshift of the mean.

Microtubule assays

For microtubule regrowth assay, mIMCD3 cells were treated with 50µM of nocodazole diluted in complete medium for 1 hour at 37°C and washed with fresh complete medium during indicated time. For low dose nocodazole treatment, mIMCD3 cells were treated for 1 hour with 100nM of nocodazole diluted in complete medium.

Zebrafish transgenic strains

Adult zebrafish were maintained at 28.5°C under standard protocols. *Tg(wt1b:GFP)*^{li1} (57), *Tg(cldnb:lynGFP)*^{zf106} (58) transgenic lines were used to visualize glomeruli and tubules of pronephros, respectively and *Tg(col2:mCherry)*^{hu5910} (59) to label facial cartilage. Embryos were maintained at 28,5°C in embryo medium with 0.1% of methylene blue. Live embryos and larvae were photographed using a Leica M165FC microscope.

Generation of CRISPR/Cas9 *ift52*$^{-/-}$ zebrafish line

Guide RNA targeting exon3 of zebrafish ift52 (5'-CTGGTGATGCTCGGAGAAGG*AGG*-3') was designed using CRISPOR online tool (http://crispor.tefor.net) (52) and cloned into pDR274 plasmid (gift from Keith Joung, Addgene plasmid #42250) according to (60). gRNA was synthesized using MAXIscript™ T7 kit (Ambion) and wild-type Cas9 mRNA was obtained by transcription of pT3TS-nCas9n (gift from Wenbiao Chen, Addgene plasmid #46757) (61) using mMESSAGE mMACHINE™ T3 Transcription Kit (Ambion). Approximately 50pg gRNA and 700pg Cas9 RNA were injected into 1-cell stage embryos. Genotyping of adult and embryos was performed by Sanger sequencing using the following

primers: zift52_F: 5'-TGCTGAAAACCTGACAGCCA-3' and zift52_R: 5'-TGTGAGACATCCGTTCGTTCA-3'.

mRNA rescue in zebrafish embryos

Zebrafish *ift52* mRNA was synthesized from pCS2-zift52 plasmid using the mMESSAGE mMACHINE™ Sp6 Transcription Kit (Ambion). 75ng of wild-type or mutated mRNA were injected into 1-cell stage embryos issued from *ift52*$^{+/-}$ incrosses.

ACKNOWLEDGEMENTS

We are grateful to the patients and their families for their participation. We thank C. Hammond for providing us the Tg(col2:mCherry) zebrafish line, M. Piel for giving us the centrin-mCherry construct and E. Niggs for c-Nap1, cep68 and Rootletin antibodies. We greatly acknowledge Necker Cell Imaging, Necker Histology and Genomic and Bioinformatic facilities for providing expert knowledge. We thank O. Pellé (Cell sorting facility), AA. Bizet and C. Arrondel for their excellent technical assistance and advices. We acknowledge P. Bastin, C. Vesque, J. Azimzadeh and B. Delaval for their scientific inputs. Finally, we thank ML. Reilly for her precious help in manuscript correction.

This research was supported by grants from the "Agence Nationale de la Recherche" (ANR) to S.S. (2016AnBiCyst) and investments for the future programs (ANR-10-IAHY-01 to S.S. and ANR-10-IAHU-01 to M.D.), and the Fondation pour la Recherche Médicale (DEQ20130326532 to S.S.), by the Novo Nordisk Foundation (grant no. NNF15OC0014164) to E.L. and by the European Union's Seventh Framework Programme (FP7/2007-2013) under grant agreement no. 305608 (EURenOmics).

CONFLICT OF INTEREST STATEMENT

None declared

REFERENCES

1 Cole, D.G., Diener, D.R., Himelblau, A.L., Beech, P.L., Fuster, J.C. and Rosenbaum, J.L. (1998) Chlamydomonas kinesin-II-dependent intraflagellar transport (IFT): IFT particles contain proteins required for ciliary assembly in Caenorhabditis elegans sensory neurons. *J. Cell Biol.*, **141**, 993-1008.

2 Lucker, B.F., Behal, R.H., Qin, H., Siron, L.C., Taggart, W.D., Rosenbaum, J.L. and Cole, D.G. (2005) Characterization of the intraflagellar transport complex B core: direct interaction of the IFT81 and IFT74/72 subunits. *J. Biol. Chem.*, **280**, 27688-27696.

3 Taschner, M., Kotsis, F., Braeuer, P., Kuehn, E.W. and Lorentzen, E. (2014) Crystal structures of IFT70/52 and IFT52/46 provide insight into intraflagellar transport B core complex assembly. *J. Cell Biol.*, **207**, 269-282.

4 Taschner, M., Weber, K., Mourao, A., Vetter, M., Awasthi, M., Stiegler, M., Bhogaraju, S. and Lorentzen, E. (2016) Intraflagellar transport proteins 172, 80, 57, 54, 38, and 20 form a stable tubulin-binding IFT-B2 complex. *EMBO J.*, **35**, 773-790.

5 Beatson, S. and Ponting, C.P. (2004) GIFT domains: linking eukaryotic intraflagellar transport and glycosylation to bacterial gliding. *Trends Biochem. Sci.*, **29**, 396-399.

6 Wolf, M.T. (2015) Nephronophthisis and related syndromes. *Curr. Opin. Pediatr.*, **27**, 201-211.

7 Reiter, J.F. and Leroux, M.R. (2017) Genes and molecular pathways underpinning ciliopathies. *Nat. Rev. Mol. Cell Biol.*, **18**, 533-547.

8 Duran, I., Taylor, S.P., Zhang, W., Martin, J., Forlenza, K.N., Spiro, R.P., Nickerson, D.A., Bamshad, M., Cohn, D.H. and Krakow, D. (2016) Destabilization of the IFT-B cilia core complex due to mutations in IFT81 causes a Spectrum of Short-Rib Polydactyly Syndrome. *Sci. Rep.*, **6**, 34232.

9 Bizet, A.A., Becker-Heck, A., Ryan, R., Weber, K., Filhol, E., Krug, P., Halbritter, J., Delous, M., Lasbennes, M.C., Linghu, B. *et al.* (2015) Mutations in TRAF3IP1/IFT54 reveal a new role for IFT proteins in microtubule stabilization. *Nat. Commun.*, **6**, 8666.

10 Lindstrand, A., Davis, E.E., Carvalho, C.M., Pehlivan, D., Willer, J.R., Tsai, I.C., Ramanathan, S., Zuppan, C., Sabo, A., Muzny, D. *et al.* (2014) Recurrent CNVs and SNVs at the NPHP1 locus contribute pathogenic alleles to Bardet-Biedl syndrome. *Am. J. Hum. Genet.*, **94**, 745-754.

11 Beales, P.L., Bland, E., Tobin, J.L., Bacchelli, C., Tuysuz, B., Hill, J., Rix, S., Pearson, C.G., Kai, M., Hartley, J. *et al.* (2007) IFT80, which encodes a conserved intraflagellar transport protein, is mutated in Jeune asphyxiating thoracic dystrophy. *Nat. Genet.*, **39**, 727-729.

12 Arts, H.H., Bongers, E.M., Mans, D.A., van Beersum, S.E., Oud, M.M., Bolat, E., Spruijt, L., Cornelissen, E.A., Schuurs-Hoeijmakers, J.H., de Leeuw, N. *et al.* (2011) C14ORF179 encoding IFT43 is mutated in Sensenbrenner syndrome. *J. Med. Genet.*, **48**, 390-395.

13 Duran, I., Taylor, S.P., Zhang, W., Martin, J., Qureshi, F., Jacques, S.M., Wallerstein, R., Lachman, R.S., Nickerson, D.A., Bamshad, M. *et al.* (2017) Mutations in IFT-A satellite core component genes IFT43 and IFT121 produce short rib polydactyly syndrome with distinctive campomelia. *Cilia*, **6**, 7.

14 Davis, E.E., Zhang, Q., Liu, Q., Diplas, B.H., Davey, L.M., Hartley, J., Stoetzel, C., Szymanska, K., Ramaswami, G., Logan, C.V. *et al.* (2011) TTC21B contributes both causal and modifying alleles across the ciliopathy spectrum. *Nat. Genet.*, **43**, 189-196.

15 Zhang, W., Taylor, S.P., Nevarez, L., Lachman, R.S., Nickerson, D.A., Bamshad, M., Krakow, D. and Cohn, D.H. (2016) IFT52 mutations destabilize anterograde complex

assembly, disrupt ciliogenesis and result in short rib polydactyly syndrome. *Hum. Mol. Genet.*, **25**, 4012-4020.

16 Girisha, K.M., Shukla, A., Trujillano, D., Bhavani, G.S., Hebbar, M., Kadavigere, R. and Rolfs, A. (2016) A homozygous nonsense variant in IFT52 is associated with a human skeletal ciliopathy. *Clin. Genet.*, **90**, 536-539.

17 Chen, X., Wang, X., Jiang, C., Xu, M., Liu, Y., Qi, R., Qi, X., Sun, X., Xie, P., Liu, Q. *et al.* (2018) IFT52 as a Novel Candidate for Ciliopathies Involving Retinal Degeneration. *Invest. Ophthalmol. Vis. Sci.*, **59**, 4581-4589.

18 Failler, M., Gee, H.Y., Krug, P., Joo, K., Halbritter, J., Belkacem, L., Filhol, E., Porath, J.D., Braun, D.A., Schueler, M. *et al.* (2014) Mutations of CEP83 cause infantile nephronophthisis and intellectual disability. *Am. J. Hum. Genet.*, **94**, 905-914.

19 Thomas, S., Legendre, M., Saunier, S., Bessieres, B., Alby, C., Bonniere, M., Toutain, A., Loeuillet, L., Szymanska, K., Jossic, F. *et al.* (2012) TCTN3 mutations cause Mohr-Majewski syndrome. *Am. J. Hum. Genet.*, **91**, 372-378.

20 Zaghloul, N.A. and Katsanis, N. (2011) Zebrafish assays of ciliopathies. *Methods Cell Biol.*, **105**, 257-272.

21 Pathak, N., Obara, T., Mangos, S., Liu, Y. and Drummond, I.A. (2007) The zebrafish fleer gene encodes an essential regulator of cilia tubulin polyglutamylation. *Mol. Biol. Cell*, **18**, 4353-4364.

22 Tsujikawa, M. and Malicki, J. (2004) Intraflagellar transport genes are essential for differentiation and survival of vertebrate sensory neurons. *Neuron*, **42**, 703-716.

23 Krock, B.L. and Perkins, B.D. (2008) The intraflagellar transport protein IFT57 is required for cilia maintenance and regulates IFT-particle-kinesin-II dissociation in vertebrate photoreceptors. *J. Cell Sci.*, **121**, 1907-1915.

24 Tapadia, M.D., Cordero, D.R. and Helms, J.A. (2005) It's all in your head: new insights into craniofacial development and deformation. *J. Anat.*, **207**, 461-477.

25 Wada, N., Javidan, Y., Nelson, S., Carney, T.J., Kelsh, R.N. and Schilling, T.F. (2005) Hedgehog signaling is required for cranial neural crest morphogenesis and chondrogenesis at the midline in the zebrafish skull. *Development*, **132**, 3977-3988.

26 Huang, P. and Schier, A.F. (2009) Dampened Hedgehog signaling but normal Wnt signaling in zebrafish without cilia. *Development*, **136**, 3089-3098.

27 Liu, A., Wang, B. and Niswander, L.A. (2005) Mouse intraflagellar transport proteins regulate both the activator and repressor functions of Gli transcription factors. *Development*, **132**, 3103-3111.

28 Salisbury, J.L., Suino, K.M., Busby, R. and Springett, M. (2002) Centrin-2 is required for centriole duplication in mammalian cells. *Curr. Biol.*, **12**, 1287-1292.

29 Dammermann, A. and Merdes, A. (2002) Assembly of centrosomal proteins and microtubule organization depends on PCM-1. *J. Cell Biol.*, **159**, 255-266.

30 Grigoriev, I.S., Chernobelskaya, A.A. and Vorobjev, I.A. (1999) Nocodazole, vinblastine and taxol at low concentrations affect fibroblast locomotion and saltatory movements of organelles. *Membr. Cell Biol.*, **13**, 23-48.

31 Jordan, M.A., Thrower, D. and Wilson, L. (1992) Effects of vinblastine, podophyllotoxin and nocodazole on mitotic spindles. Implications for the role of microtubule dynamics in mitosis. *J. Cell Sci.*, **102 (Pt 3)**, 401-416.

32 Mayor, T., Stierhof, Y.D., Tanaka, K., Fry, A.M. and Nigg, E.A. (2000) The centrosomal protein C-Nap1 is required for cell cycle-regulated centrosome cohesion. *J. Cell Biol.*, **151**, 837-846.

33 Bahe, S., Stierhof, Y.D., Wilkinson, C.J., Leiss, F. and Nigg, E.A. (2005) Rootletin forms centriole-associated filaments and functions in centrosome cohesion. *J. Cell Biol.*, **171**, 27-33.

34 Graser, S., Stierhof, Y.D. and Nigg, E.A. (2007) Cep68 and Cep215 (Cdk5rap2) are required for centrosome cohesion. *J. Cell Sci.*, **120**, 4321-4331.

35 Floriot, S., Vesque, C., Rodriguez, S., Bourgain-Guglielmetti, F., Karaiskou, A., Gautier, M., Duchesne, A., Barbey, S., Fritz, S., Vasilescu, A. *et al.* (2015) C-Nap1 mutation affects centriole cohesion and is associated with a Seckel-like syndrome in cattle. *Nat. Commun.*, **6**, 6894.

36 Euteneuer, U. and Schliwa, M. (1985) Evidence for an involvement of actin in the positioning and motility of centrosomes. *J. Cell Biol.*, **101**, 96-103.

37 Jean, C., Tollon, Y., Raynaud-Messina, B. and Wright, M. (1999) The mammalian interphase centrosome: two independent units maintained together by the dynamics of the microtubule cytoskeleton. *Eur. J. Cell Biol.*, **78**, 549-560.

38 Panic, M., Hata, S., Neuner, A. and Schiebel, E. (2015) The centrosomal linker and microtubules provide dual levels of spatial coordination of centrosomes. *PLoS Genet.*, **11**, e1005243.

39 Halbritter, J., Bizet, A.A., Schmidts, M., Porath, J.D., Braun, D.A., Gee, H.Y., McInerney-Leo, A.M., Krug, P., Filhol, E., Davis, E.E. *et al.* (2013) Defects in the IFT-B component IFT172 cause Jeune and Mainzer-Saldino syndromes in humans. *Am. J. Hum. Genet.*, **93**, 915-925.

40 Tory, K., Lacoste, T., Burglen, L., Moriniere, V., Boddaert, N., Macher, M.A., Llanas, B., Nivet, H., Bensman, A., Niaudet, P. *et al.* (2007) High NPHP1 and NPHP6 mutation rate in patients with Joubert syndrome and nephronophthisis: potential epistatic effect of NPHP6 and AHI1 mutations in patients with NPHP1 mutations. *J. Am. Soc. Nephrol.*, **18**, 1566-1575.

41 Ryan, R., Failler, M., Reilly, M.L., Garfa-Traore, M., Delous, M., Filhol, E., Reboul, T., Bole-Feysot, C., Nitschke, P., Baudouin, V. *et al.* (2018) Functional characterization of tektin-1 in motile cilia and evidence for TEKT1 as a new candidate gene for motile ciliopathies. *Hum. Mol. Genet.*, **27**, 266-282.

42 Katsanis, N., Ansley, S.J., Badano, J.L., Eichers, E.R., Lewis, R.A., Hoskins, B.E., Scambler, P.J., Davidson, W.S., Beales, P.L. and Lupski, J.R. (2001) Triallelic inheritance in Bardet-Biedl syndrome, a Mendelian recessive disorder. *Science*, **293**, 2256-2259.

43 Leitch, C.C., Zaghloul, N.A., Davis, E.E., Stoetzel, C., Diaz-Font, A., Rix, S., Alfadhel, M., Lewis, R.A., Eyaid, W., Banin, E. *et al.* (2008) Hypomorphic mutations in syndromic encephalocele genes are associated with Bardet-Biedl syndrome. *Nat. Genet.*, **40**, 443-448.

44 Wilson, F.H., Disse-Nicodeme, S., Choate, K.A., Ishikawa, K., Nelson-Williams, C., Desitter, I., Gunel, M., Milford, D.V., Lipkin, G.W., Achard, J.M. *et al.* (2001) Human hypertension caused by mutations in WNK kinases. *Science*, **293**, 1107-1112.

45 Townsley, F.M., Aristarkhov, A., Beck, S., Hershko, A. and Ruderman, J.V. (1997) Dominant-negative cyclin-selective ubiquitin carrier protein E2-C/UbcH10 blocks cells in metaphase. *Proc. Natl. Acad. Sci. U S A*, **94**, 2362-2367.

46 Lindstrom, N.O., De Sena Brandine, G., Tran, T., Ransick, A., Suh, G., Guo, J., Kim, A.D., Parvez, R.K., Ruffins, S.W., Rutledge, E.A. *et al.* (2018) Progressive Recruitment of Mesenchymal Progenitors Reveals a Time-Dependent Process of Cell Fate Acquisition in Mouse and Human Nephrogenesis. *Dev. Cell*, **45**, 651-660 e654.

47 Rachel, R.A., May-Simera, H.L., Veleri, S., Gotoh, N., Choi, B.Y., Murga-Zamalloa, C., McIntyre, J.C., Marek, J., Lopez, I., Hackett, A.N. *et al.* (2012) Combining Cep290 and Mkks ciliopathy alleles in mice rescues sensory defects and restores ciliogenesis. *J. Clin. Invest.*, **122**, 1233-1245.

48 Delaval, B., Bright, A., Lawson, N.D. and Doxsey, S. (2011) The cilia protein IFT88 is required for spindle orientation in mitosis. *Nat. Cell Biol.*, **13**, 461-468.

49 Fischer, E., Legue, E., Doyen, A., Nato, F., Nicolas, J.F., Torres, V., Yaniv, M. and Pontoglio, M. (2006) Defective planar cell polarity in polycystic kidney disease. *Nat. Genet.*, **38**, 21-23.

50 Pradeep, J., Sambashivaiah, S., Thomas, T., Radhakrishnan, R., Vaz, M. and Srinivasan, K. (2012) Heart rate variability responses to standing are attenuated in drug naive depressed patients. *Indian J. Physiol. Pharmacol.*, **56**, 213-221.

51 Taschner, M., Bhogaraju, S., Vetter, M., Morawetz, M. and Lorentzen, E. (2011) Biochemical mapping of interactions within the intraflagellar transport (IFT) B core complex: IFT52 binds directly to four other IFT-B subunits. *J. Biol. Chem.*, **286**, 26344-26352.

52 Haeussler, M., Schonig, K., Eckert, H., Eschstruth, A., Mianne, J., Renaud, J.B., Schneider-Maunoury, S., Shkumatava, A., Teboul, L., Kent, J. *et al.* (2016) Evaluation of off-target and on-target scoring algorithms and integration into the guide RNA selection tool CRISPOR. *Genome Biol.*, **17**, 148.

53 Ran, F.A., Hsu, P.D., Wright, J., Agarwala, V., Scott, D.A. and Zhang, F. (2013) Genome engineering using the CRISPR-Cas9 system. *Nat. Protoc.*, **8**, 2281-2308.

54 Kishore, S., Khanna, A. and Stamm, S. (2008) Rapid generation of splicing reporters with pSpliceExpress. *Gene*, **427**, 104-110.

55 Cox, J. and Mann, M. (2008) MaxQuant enables high peptide identification rates, individualized p.p.b.-range mass accuracies and proteome-wide protein quantification. *Nat. Biotechnol.*, **26**, 1367-1372.

56 Luber, C.A., Cox, J., Lauterbach, H., Fancke, B., Selbach, M., Tschopp, J., Akira, S., Wiegand, M., Hochrein, H., O'Keeffe, M. *et al.* (2010) Quantitative proteomics reveals subset-specific viral recognition in dendritic cells. *Immunity*, **32**, 279-289.

57 Perner, B., Englert, C. and Bollig, F. (2007) The Wilms tumor genes wt1a and wt1b control different steps during formation of the zebrafish pronephros. *Dev. Biol.*, **309**, 87-96.

58 Haas, P. and Gilmour, D. (2006) Chemokine signaling mediates self-organizing tissue migration in the zebrafish lateral line. *Dev. Cell*, **10**, 673-680.

59 Hammond, C.L. and Schulte-Merker, S. (2009) Two populations of endochondral osteoblasts with differential sensitivity to Hedgehog signalling. *Development*, **136**, 3991-4000.

60 Hwang, W.Y., Fu, Y., Reyon, D., Maeder, M.L., Tsai, S.Q., Sander, J.D., Peterson, R.T., Yeh, J.R. and Joung, J.K. (2013) Efficient genome editing in zebrafish using a CRISPR-Cas system. *Nat. Biotechnol.*, **31**, 227-229.

61 Jao, L.E., Wente, S.R. and Chen, W. (2013) Efficient multiplex biallelic zebrafish genome editing using a CRISPR nuclease system. *Proc. Natl. Acad. Sci. U S A*, **110**, 13904-13909.

LEGENDS TO FIGURES

Figure 1 : Identification and characterization of novel *IFT52* mutations.

(A-B) Pedigrees (A) and chromatograms (B) of Families 1 and 2 showing the segregation of novel *IFT52* mutations. Arrowheads in chromatograms indicate mutations shown below the wild-type sequence. SB, stillbirth; wk, week; n, unknown number of unaffected children.

(C) Clinical features of foetuses F1:II-1 (C1-C2) and F2:II-3 (C4-C5). Radiographies from F1:II-1 show polydactyly (asterisks) in right arm (C1) and lower limbs (C2). Kidney sections of age-matched control (C3) and F2:II-3 proband (C4) were stained with hematoxylin-eosin (HE) and HE-saffron, respectively. C4 shows a voluminous kidney with numerous cysts, that is three to four times bigger than the age-matched control kidney (C3). Higher magnifications show the nephrogenic zone in the cortex area of control kidney (C3') whereas in F2:II-3 proband, cyst (asterisk) is surrounded by immature loose mesenchymal tissue with no differentiated renal structure or nephrogenic blastema (C4'). Radiography from F2:II-3 (C5) shows the absence of skeletal defects. Scale bars, 5mm (C3-C4) and 500µm (C3'-C4').

(D) Analysis of the effect of c.695_699delinsCA mutation on splicing by minigene approach. gDNA sequences of exon8 and flanking introns were cloned in pSpliceExpress vector between exons 2 and 3 of the rat *Insulin* (*Ins*) gene (upper panel). Arrows indicate the positions of the primers used for RT-PCR, so that correct splicing of exon8 resulted into a PCR product of 322pb. RT-PCR performed from HEK293 cell extracts transfected with pSpliceExpress constructs containing gDNA from the mother F1:I-1 or the foetus F1:II-3 (lower panel). Arrowhead shows the expected PCR product for F1:I-1 sample whereas additional lower bands were detected in F1:II-3 sample.

(E) Inter-species protein sequence alignment (Clustal Omega) shows the high conservation of Asn98 (N98) and Asp259 (D259) amino acids throughout evolution.

(F-H) RT-PCR (F) and western blot (G) from fibroblast extracts of control (Ctrl) and Family 3 patient (F3-Pt). c.424C>T mutation results in partial skipping of the exon 6 (F) that leads to the expression of a shorter protein depleted of 24 amino acids (expected size of 47kDa) (G). Quantification of IFT52 protein levels indicates a drastic decrease of IFT52 expression in Family 3 patient (H) (mean ± s.e.m of n=3 experiments; *p<0.01, t-test).

(I-J) Exon structure (JI and protein domains (J) of human IFT52 showing the positions of all reported *IFT52* mutations (our study and referenced publications) in the N-terminal GIFT domain.

Figure 2 : Validation of the effect of *IFT52* missense mutations in zebrafish.

(A-B) Global morphology of wild-type, heterozygous (WT/het, A) and *ift52* mutant (B) embryos at 48hpf shows the ventral body curvature in homozygous mutant animals (B).

(C-D) Images of *Tg(wt1b:GFP)*-labeled proximal pronephros of WT/het and *ift52* mutant embryos at 48hpf. Asterisks indicate cysts in glomeruli (D). Dorsal views, anterior to the left. Scale bar, 50µm.

(E-F) Confocal images of nasal pits of WT/het (E) and *ift52* mutant (F) embryos at 72hpf. Cilia (acetylated α-tubulin, white) are visible at the apical surface (phalloidin, red) of WT/het olfactive bulbs (E). Scale bar, 25µm.

(G-H) Confocal images of *Tg(cldnb:lynGFP)*-labeled pronephros of WT/het (G, G') and *ift52* mutant (H, H') embryos at 72hpf. Patches of cilia (acetylated α-tubulin) of multiciliated cells are visible in WT/het (G') embryos while only cilia of monociliated cells remained in mutant embryos (H'). Ventral views, anterior to the left. Scale bar, 25µm.

(I-J) Percentage of *ift52*$^{-/-}$ embryos displaying ventral body curvature (I) and pronephric cysts (J) at 48 hpf, after injection of zebrafish WT (blue), D259H- (orange) or N98S- (purple) mutated *ift52* RNA. Graph shows the mean ± s.e.m of n=3 experiments (total number of

embryos=30). $^{\S}p<0.05$, comparing to non-injected (-) *Ift52* mutant (ANOVA followed by Dunn's post-hoc test). ns, non-significant.

Figure 3 : Missense *IFT52* mutations affect ciliogenesis *in vitro*

(A) Confocal images of parental control IMCD3 cells and CRISPR/Cas9-derived *Ift52*$^{-/-}$ clonal cell line expressing GFP alone, WT or mutated GFP-tagged murine Ift52. Cilia are labelled with acetylated α-tubulin (red), centrosome with γ-tubulin (white). Scale bar, 5µm.

(B) Quantification of the percentage of ciliated cells in (A). Graph shows the mean ± s.e.m. of at least 3 independent experiments (n>150 cells for each experiment). $^{\S\S\S}p<0.001$ comparing to *Ift52*$^{-/-}$ cell line, ***p<0.001 comparing to WT GFP-Ift52 expressing cell line, $^{\#\#\#}p<0,001$ (ANOVA followed by Kruskall-Wallis post-hoc test). ns, non-significant.

(C) Quantification of cilia length according to acetylated α-tubulin staining in (A). Violin plots show the frequency of each cilium length, with the black point indicating the mean value ± SD and the red dashed line the mean value of WT GFP-Ift52 expressing cell line. Values are from at least 3 independent experiments (n>100 cilia for each experiment). **p<0.01 and ***p<0.001 comparing to WT GFP-Ift52 expressing cell line, $^{\#\#}p<0.01$ and $^{\#\#\#}p<0.001$ (ANOVA followed by Kruskall-Wallis post-hoc test).

(D) Confocal images of serum starved fibroblasts from age-matched controls (Ctrl 1 and Ctrl2) and Family 3 patient (F3-Pt). Cilia are stained with acetylated α-tubulin (red) and centrosome with γ-tubulin (green). Insets show higher magnifications of representative cilia. Scale bar, 10µm.

(E) Quantification of the percentage of ciliated cells in (D). Graph shows the mean ± s.e.m of at least 3 independent experiments (n>35 cells for each experiment). *p<0.05, ANOVA followed by Dunn's post-hoc test.

(F) Quantification of cilia length according to acetylated α-tubulin staining in (D). Violin plots show the frequency of each cilium length, with the white point indicating the mean value ± SD and the red dashed line the mean value of Ctrl1 cell line. Values are from at least 3 independent experiments (n>35 cells for each experiment). **p<0.01 and ***p<0.001, ANOVA followed by Dunn's post-hoc test.

Figure 4 : Missense *IFT52* mutations alter IFT-B2 subunit interaction and localisation

(A) Crystal structure of the N-terminal GIFT domain of *Chlamydomonas reinhardtii* (Cr, green) and *Mus musculus* (Mm, cyan) are superposed and shown in a cartoon represention in two perpendicular views. IFT52 mutations are shown as sticks. The black boxes show zoom in on the MmIFT52 structure, only highlighting the N98 residue (left box) and the I233/M234 residues (mouse sequence, right box). Whereas N98 forms two hydrogen bonds with backbone atoms of F65, the I233 and M234 residues are part of two hydrophobic cores of the GIFT domain.

(B-D) Volcano plots showing significant IFT-B subunit interactions (filled blue/green spots) with immunoprecipitated WT (A), D259H-mutated (B) and N98S-mutated (C) GFP-Ift52 protein compared with immunoprecipitated GFP alone. Insignificant IFT-B subunit interactions are indicated by filled grey/dark green spots. Data are from 5 independent experiments.

(E) Co-immunoprecipitation assays of GFP-tagged WT and mutated Ift52 proteins with the direct partners Ift38 and Ift57.

(F) Quantification of relative levels of co-immunoprecipitated Ift38 (plain bars) and Ift57 (dashed bars). Values are normalized to that of WT GFP-Ift52. Graph shows mean ± s.e.m. of n=3 independent experiments. ***p<0.001 comparing to WT GFP-Ift52 immunoprecipitates, $^{\#}$p<0.05, $^{\#\#}$p<0.01 and $^{\#\#\#}$p<0.001 (ANOVA followed by Dunn's post-hoc test).

(G) Confocal images of WT and mutated GFP-tagged Ift52 localization. Cilia are labelled with acetylated α-tubulin (red) and centrosome with γ-tubulin (white). Scale bar, 2.5µm.

(H) Quantification of relative levels of ciliary Ift52 shown in (G). Graph shows the mean ± s.e.m. of n=3 independent experiments (n>30 cells for each experiment). ***p<0.001 comparing to WT GFP-Ift52, $^{###}$p<0.001 (ANOVA followed by Dunn's post-hoc test). ns, non-significant.

(I) Confocal images of Ift38 (white) localization in WT- and mutated GFP-Ift52 expressing cell lines. Cilia are labelled with acetylated α-tubulin (red) and centrosome with γ-tubulin (green). Scale bar, 5µm.

(J) Quantification of relative levels of ciliary Ift38 (plain bars) and Ift57 (dashed bars) shown in (I). Values are normalized to that of WT GFP-Ift52. Graph shows the mean ± s.e.m. of n=3 independent experiments (n>30 cells for each experiment). $^{#}$p<0.05, ANOVA followed by Dunn's post-hoc test.

<u>Figure 5 :</u> Ift52 interacts and colocalises with centrin at the distal end of centrioles

(A-B) Confocal images and schema of GFP-Ift52 (green) localization at the centrosome. Proximal end of father centriole is labelled with c-Nap1 (red) (A) and distal end of centrioles with centrin (red) (B, B'). γ-tubulin staining (white) shows the proximal part of the centrioles (B, B'). Scale bar, 1.5µm.

(C) Co-immunoprecipitation assays of WT and mutated GFP-tagged Ift52 proteins with mCherry-tagged centrin. GFP-Ift52 and centrin-mCherry constructs were co-transfected in HEK293T cells.

(D) Quantification of relative levels of co-immunoprecipitated centrin-mCherry. Values are normalized to that of WT GFP-Ift52. Graph shows mean ± s.e.m. of n=3 independent experiments. ns, non-significant.

(E-F) Confocal images (E) and quantification (F) of endogenous centrin (red, E) localization in parental control IMCD3 cells, *Ift52*$^{-/-}$ and WT GFP-Ift52 expressing cell lines. Centrosome is labelled with γ-tubulin (green, E). Graph (F) shows the mean ± s.e.m. of n=3 independent experiments. *p<0.05, ANOVA followed by Dunn's post-hoc test. ns, non-significant. Scale bar, 5μm.

Figure 6 : *Ift52*$^{-/-}$ IMCD3 cells show defective microtubule anchorage and dynamics

(A) Confocal images of microtubule regrowth assay in parental control IMCD3 cells, *Ift52*$^{-/-}$ and WT GFP-Ift52 expressing cell lines. Cells were treated with 50μM nocodazole for 1 hour (T0), followed by drug removal for 5 (T+5min) or 10 (T+10min) minutes. Arrows indicate free, unanchored to the centrosome, microtubules. Scale bars, 10μm and 1μm for magnification.

(B) Quantification of aster area of microtubules at T+10min, according to a-tubulin staining shown in (A). Values are normalized to that of parental control IMCD3 cells. Graph shows the mean ± s.e.m. of n=3 independent experiments. *** p < 0.001, ANOVA followed by Dunn's post-hoc test.

(C) Confocal images of plus-end microtubule marker EB1 (red) in parental control IMCD3 cells, *Ift52*$^{-/-}$ and WT GFP-Ift52 expressing cell lines. Scale bar, 5μm (magnification scale bar 2.5μm).

(D) Quantification of EB1-positive comet length, according to EB1 staining in (C). Graph show mean ± s.e.m of n=3 independent experiments (around 500 comets total). **p<0.01, ***p<0.001, ANOVA followed by Dunn's post-hoc test.

(E) Confocal images of cytoplasmic microtubules in parental control IMCD3 cells, *Ift52*$^{-/-}$ and WT GFP-Ift52 expressing cell lines, following a low dose (100nM) nocodazole treatment of 1

hour (T+1h). Cytoplasmic microtubules are labelled with α-tubulin and stabilized microtubules with acetylated α-tubulin. NT, non-treated. Scale bar, 10µm.

(F) Confocal images of *Tg(cldnb:lynGFP)*-labeled pronephros of WT/het and *ift52* mutant embryos at 72hpf. Acetylated α-tubulin labels cilia as well as stabilized cytoplasmic microtubules (arrowheads). Ventral views, anterior to the left. Scale bar, 10µm.

Figure 7 : *Ift52*$^{-/-}$ IMCD3 cells exhibit centriole splitting

(A) Quantification of the distance between the two centrioles, according to γ-tubulin staining in Figure 3A. Box plots show median and 1st and 3rd quartiles of n=4 independent experiments. $^{§}p<0.05$, $^{§§§}p<0.001$ comparing to parental control IMCD3 cells, ***p<0.001 comparing to WT GFP-Ift52 expressing cell line (ANOVA followed by Kruskall-Wallis post-hoc test).

(B) Confocal images of split centrosome (green) in parental control cells and *Ift52*$^{-/-}$ and WT GFP-Ift52 expressing cell lines, following transfection of low dose of c-Nap1-targeting siRNA. Luciferase (Luc.) targeting siRNA was used as a control. Scale bar, 2.5µm.

(C) Quantification of centriole distance according to γ-tubulin staining shown in (B). Box plots show the mean and 1st and 3rd quartiles of n=3 independent experiments. ***p<0.001, ANOVA followed by Dunn's post-hoc test.

Figure S1 : Generation of *ift52*^{ii003} zebrafish line using CRISPR/Cas9 technology

(A) Chromatograms of genomic DNAs and related amino acid sequences of WT and *ift52*^{ii003} zebrafish embryos. Sequence of guide RNA is indicated with a black line. Red square highlights the deletion of 4 nucleotides in WT sequence that results in a frameshift and premature stop codon (c.266_269delAGGA; p.E89fs91*) in *ift52*^{ii003} line.

(B) Representative clutch of 48hpf embryos issued from *ift52*$^{+/-}$ zebrafish incrosses. Scale bar, 1mm.

(C) Images of *Tg(col2a:mCherry)*-labeled craniofacial cartilage of WT/het and *ift52*$^{-/-}$ larvae at 4dpf. Yellow arrows indicate the distance between the Meckel's cartilage and hyoid arches. Ventral views, anterior to the left. Scale bar, 200µm.

(D) Quantification of the distance between Meckel's cartilage and hyoid arches shown in (C). Graph shows the mean ± s.e.m of n=3 independent clutches (total number of embryos=30). ***p<0.001, t-test with Welch's correction.

(E) Relative q-PCR analysis of mRNA expression of Hedgehog target genes *ptc1, ptc2* and *gli1* in WT/het and *ift52*$^{-/-}$ heads at 4dpf. Graph shows the mean ± s.e.m of n=2 independent experiments.

<u>Figure S2 :</u> Generation of *Ift52*$^{-/-}$ mIMCD3 cell line using CRISPR/Cas9 technology

(A) Chromatograms of genomic DNAs and related amino acid sequences of WT and *Ift52*$^{-/-}$ mIMCD3 cell lines. Sequence of guide RNA is indicated with a black line. Red square highlights the deletion of 5 nucleotides in WT sequence that results in a frameshift and premature stop codon (c.170_174delTCACA; p.Ile57Serfs66*) in *Ift52*$^{-/-}$ line.

(B) Western blot showing the loss of expression of endogenous Ift52 protein in *Ift52*$^{-/-}$ cells and the expression of GFP alone or GFP-tagged WT-, D259H-, N98S- and Δex6-Ift52 after lentiviral infection.

(C) SDS-PAGE gel demonstrating that WT, N98S and IMdelT mutant IFT52 (1-335) constructs containing the GIFT domain and the following IFT88-binding region can be over-expressed in *E.coli*. The His-tag pulldown (right panel) shows that the WT construct is perfectly soluble whereas the IMdelT mutant IFT52 is not soluble at all and the N98S mutant

IFT52 is only soluble to a small degree. The lack of solubility may be a result of mis-folding and aggregation and/or instability and degradation of the mutant constructs.

(D) Co-expression of WT and mutant His-GST-tagged IFT52 (1-335) with Sumo-tagged IFT88. The pull-down experiment shows that whereas WT IFT52 (1-335) is soluble and pulls down IFT88. Interestingly, the N98S mutant IFT52 construct is stabilized by and pulls down IFT88. In contrast, the IMdelT mutant IFT52 is only stabilized to a small degree by co-expression with the IFT88 construct.

(E) Size exclusion chromatography (SEC) of WT (blue), N98S (green) and IMdelT (red) CrIFT52 in complex with CrIFT88. The N98S mutant elutes at approximately the same volume as WT but at a much lower yield and a less symmetric elution profile suggesting folding/stability problems.

(F-G) Confocal images of endogenous Ift52 (red) localisation at the centrosome (green, arrowheads) in non-ciliated cells (E') and along the cilium (cyan, arrow) (E''), as well as at the spindle poles (F) in wild-type IMCD3 cells. Scale bar, 5μm.

Figure S3 : Effects of the missense mutations on protein linker components

(A-B) Confocal images of Ki67 staining (A) and quantification (B) of Ki67-positive cells in parental control IMCD3 cells and *Ift52*$^{-/-}$ and WT GFP-Ift52 expressing cell lines. Scale bar, 10μm.

(C) Confocal images of the localisation of components of the protein linker, c-Nap1, Rootletin, cep68 and LRRC45 (white), in parental control cells and *Ift52*$^{-/-}$ and WT GFP-Ift52 expressing cell lines. γ-tubulin (green) labels the centrosome. Insets at the lower left show higher magnifications of representative centrosome. Scale bar, 2μm.

(D-E) Quantification of c-Nap1 (D) and rootletin (E) intensity staining at the centrosome as in (C). Graph shows the mean ± s.e.m. of n=3 independent experiments.

Table 1 : Mutations in *IFT52* and associated clinical features

Family	Patient	nt change[a]	aa change	Exon	Parental consanguinity	Age	Renal phenotype	Skeletal phenotype	Ocular phenotype	Other	Reference
F1	II-1	c.293A>G (het) c.695-699delinsCA (het)	p.N98S p.I232M233delinsT	4 8	No	23 wks	Tortuous ureters and left pelviectasis	SRP syndrome Short ribs, narrow chest, short long bones, polydactyly of both hands and right foot	-	-	This study
	II-3	c.293A>G (het) c.695-699delinsCA (het)	p.N98S p.I232M233delinsT	4 8	No	16 wks	No	SRP syndrome Mild rib shortening, small rib cage, post axial polydactyly of both hands and left foot	-	-	This study
F2	II-4	c.775G>C (hom)	p.D259H	10	Yes	20,5 wks	Multicystic dyplastic kidneys (no differenciated kidney structure and voluminous cysts)	No	-	-	This study
F3		c.424C>T (hom)	p.R142*/Δex6	6	Yes	3 yrs	No (at the time of the publication)	Sensenbrenner syndrome Narrow thorax, short limbs, dolichocephaly, tall forehead, telecanthus, mid-face hypoplasia, small and spaced teeth, brachydactyly of hands and feet, bilateral postaxial polydactyly	Pigmentary retinopathy nystagmus	Hypoplastic corpus callosum	Girisha et al., 2016
F4		c.595A>G (het) c.878delT (het)	p.A199T p.L293Afs21*	7 10	No	20/23 wks	No	SRP syndrome Narrow thorax, mild rib shortening, reverse campomelia of humeri, mild bent of femurs, no polydactyly	-	-	Zhang et al, 2016
F5		c.556A>G (hom)	p.T186A	7	Yes	11 yrs	No (at the time of the publication)	Sensenbrenner syndrome Narrow chest, short ribs, micromelic limbs, severe growth delay, dental dysplasia	Leber Congenital Amaurosis nystagmus	Mild mental retardation	Chen et al. 2018

Abbreviations are as follows: nt, nucleotide; aa, amino acid; hom, homozygous; het, heterozygous; wks, weeks; yrs, years; SRP, Short Rib-Polydactyly.
[a]cDNA mutations are numbered according to human cDNA reference sequence GenBank:NM_016004.2 (IFT52), where +1 corresponds to the A of ATG start translation codon.

ABBREVIATIONS

SRTD: Short-Rib Thoracic Dysplasia

IFT: Intraflagellar Transport

WES: Whole Exome Sequencing

CAKUT: Congenital Anomalies of Kidney and Urinary Tract

SIFT: Sorting Intolerant From Tolerant

CADD: Combined Annotation Dependent Depletion

hpf: hours post fertilisation

het: heterozygous

Hh: Hedgehog

IMCD3: Inner Medullar Collecting Duct

FIGURE 1

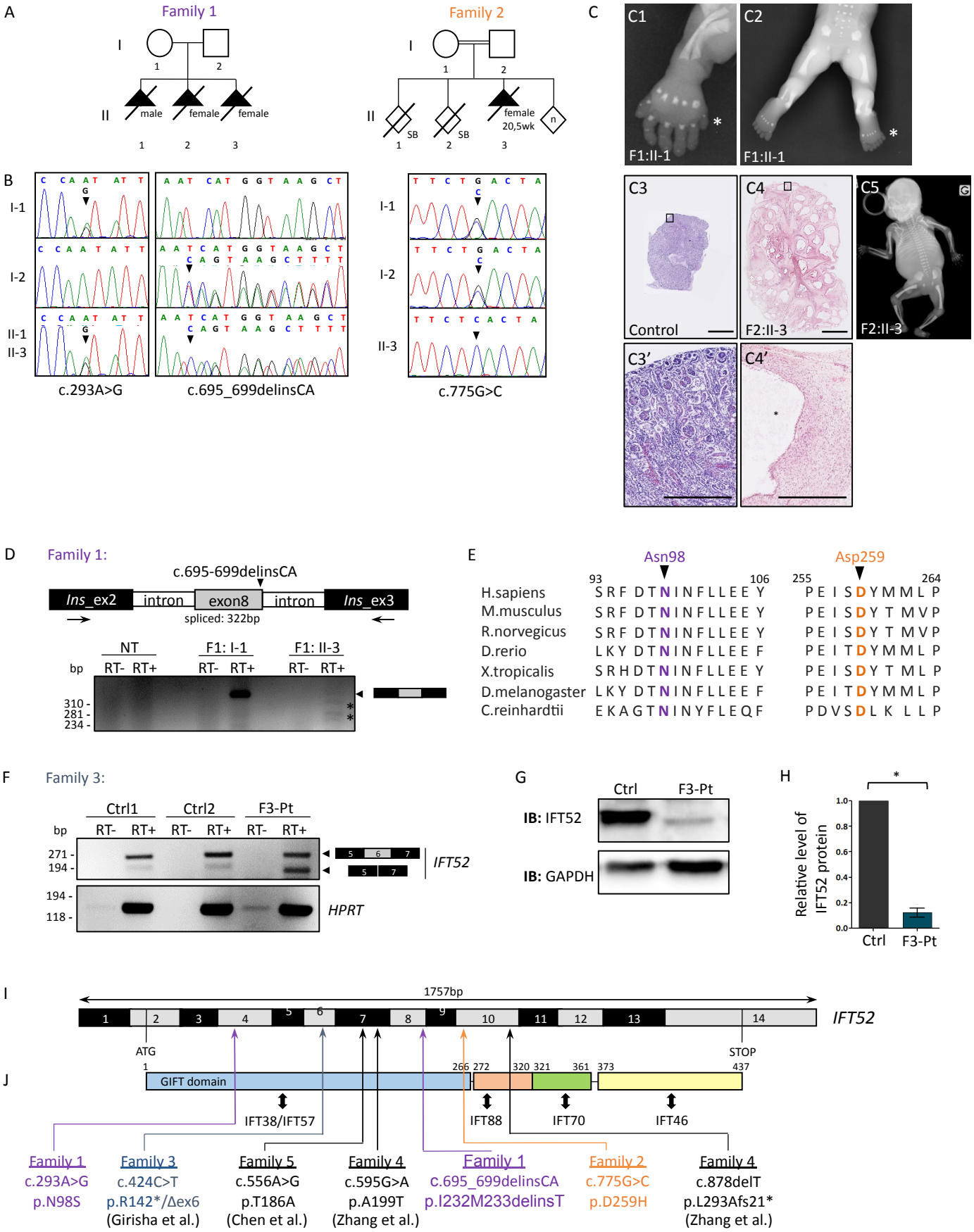
A
Family 1
I
1
2
II
male
female
female
1
2
3
Family 2
I
1
2
II
SB
SB
female
20,5wk
n
1
2
3
B
I-1
I-2
II-1
II-3
c.293A>G
c.695_699delinsCA
I-1
I-2
II-3
c.775G>C
C
C1
F1:II-1
C2
F1:II-1
C3
Control
C4
F2:II-3
C5
F2:II-3
C3'
C4'
D
Family 1:
c.695-699delinsCA
Ins_ex2
intron
exon8
intron
Ins_ex3
spliced: 322bp
NT
F1: I-1
F1: II-3
bp
RT- RT+
RT- RT+
RT- RT+
310 -
281 -
234 -
E
Asn98
Asp259
93
106
255
264
H.sapiens S R F D T N I N F L L E E Y P E I S D Y M M L P
M.musculus S R F D T N I N F L L E E Y P E I S D Y T M V P
R.norvegicus S R F D T N I N F L L E E Y P E I S D Y T M V P
D.rerio L K Y D T N I N F L L E E F P E I T D Y M M L P
X.tropicalis S R H D T N I N F L L E E Y P E I S D Y T M L P
D.melanogaster L K Y D T N I N F L L E E F P E I T D Y M M L P
C.reinhardtii E K A G T N I N Y F L E Q F P D V S D L K L L P
F
Family 3:
Ctrl1
Ctrl2
F3-Pt
bp
RT- RT+ RT- RT+ RT- RT+
271 -
194 -
5 6 7
5 7
IFT52
194 -
118 -
HPRT
G
Ctrl
F3-Pt
IB: IFT52
IB: GAPDH
H
*
Relative level of IFT52 protein
1.0
0.8
0.6
0.4
0.2
0.0
Ctrl
F3-Pt
I
1757bp
1
2
3
4
5
6
7
8
9
10
11
12
13
14
IFT52
ATG
1
STOP
437
J
GIFT domain
266 272
320 321
361
373
IFT38/IFT57
IFT88
IFT70
IFT46
Family 1
c.293A>G
p.N98S
Family 3
c.424C>T
p.R142*/Δex6
(Girisha et al.)
Family 5
c.556A>G
p.T186A
(Chen et al.)
Family 4
c.595G>A
p.A199T
(Zhang et al.)
Family 1
c.695_699delinsCA
p.I232M233delinsT
Family 2
c.775G>C
p.D259H
Family 4
c.878delT
p.L293Afs21*
(Zhang et al.)

FIGURE 2

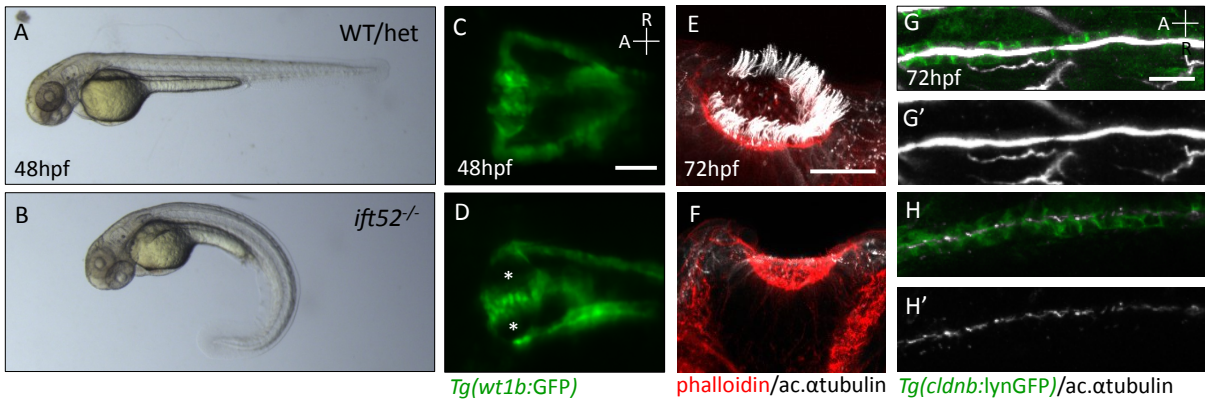
A
WT/het
48hpf
B
ift52-/-
C
R
A
48hpf
D
*
*
E
72hpf
F
G
A
72hpf
G'
H
H'
Tg(wt1b:GFP)
phalloidin/ac.αtubulin
Tg(cldnb:lynGFP)/ac.αtubulin

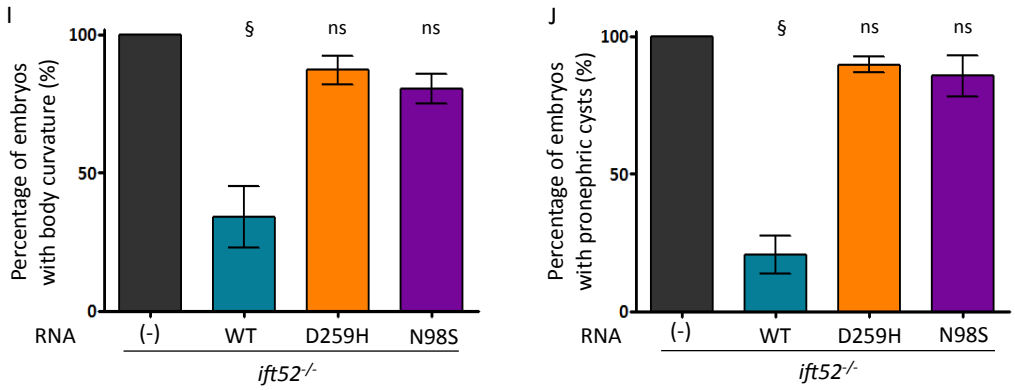
I
Percentage of embryos with body curvature (%)
100
50
0
§
ns
ns
RNA
(-)
WT
D259H
N98S
ift52-/-
J
Percentage of embryos with pronephric cysts (%)
100
50
0
§
ns
ns
RNA
(-)
WT
D259H
N98S
ift52-/-

FIGURE 3

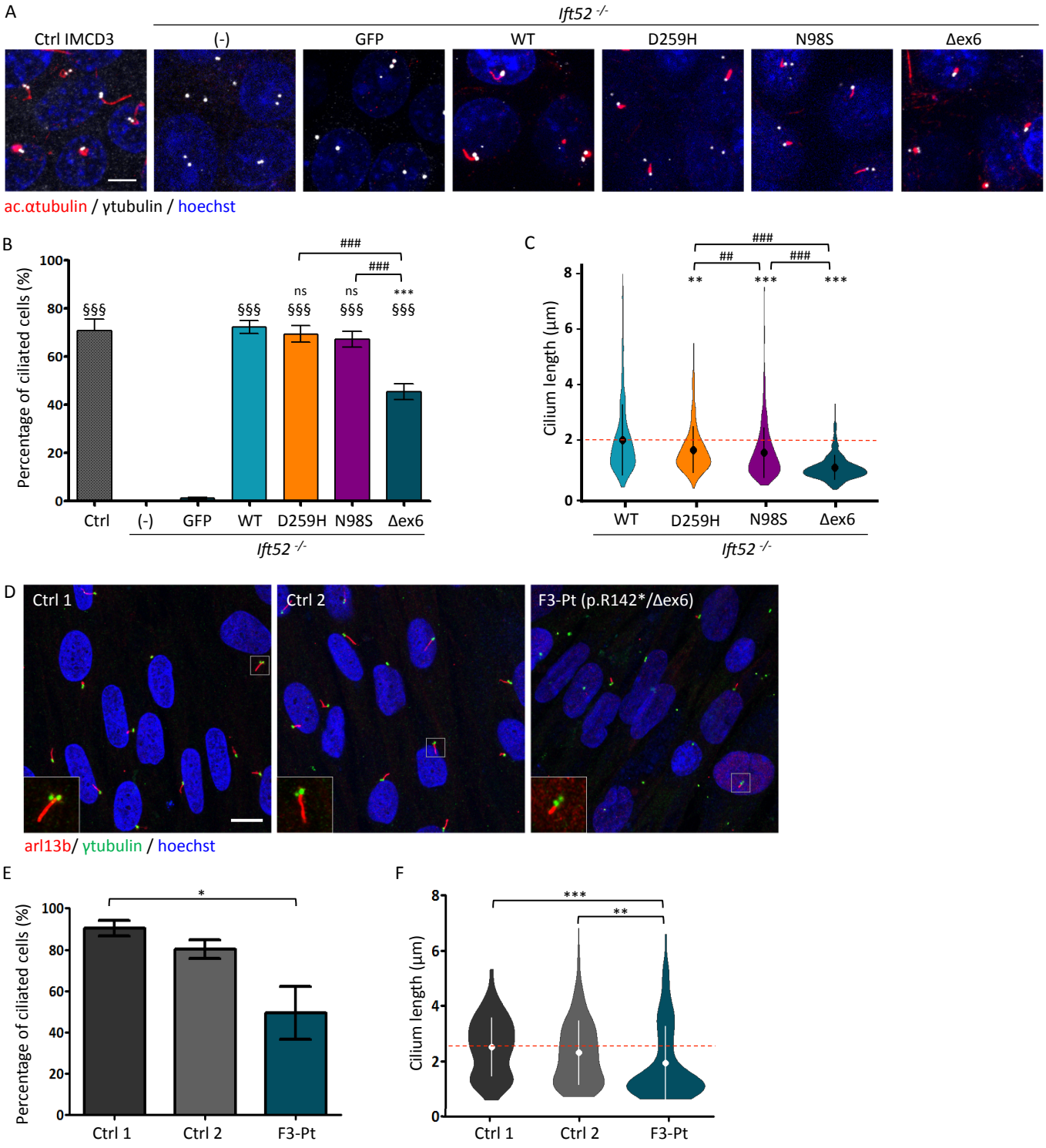
A
Ift52 -/-
Ctrl IMCD3
(-)
GFP
WT
D259H
N98S
Δex6
ac.αtubulin / γtubulin / hoechst
B
Percentage of ciliated cells (%)
§§§
ns
***
###
Ctrl
(-)
GFP
WT
D259H
N98S
Δex6
Ift52 -/-
C
Cilium length (µm)
##
**
WT
D259H
N98S
Δex6
Ift52 -/-
D
Ctrl 1
Ctrl 2
F3-Pt (p.R142*/Δex6)
arl13b/ γtubulin / hoechst
E
Percentage of ciliated cells (%)
*
Ctrl 1
Ctrl 2
F3-Pt
F
Cilium length (µm)
Ctrl 1
Ctrl 2
F3-Pt

FIGURE 4

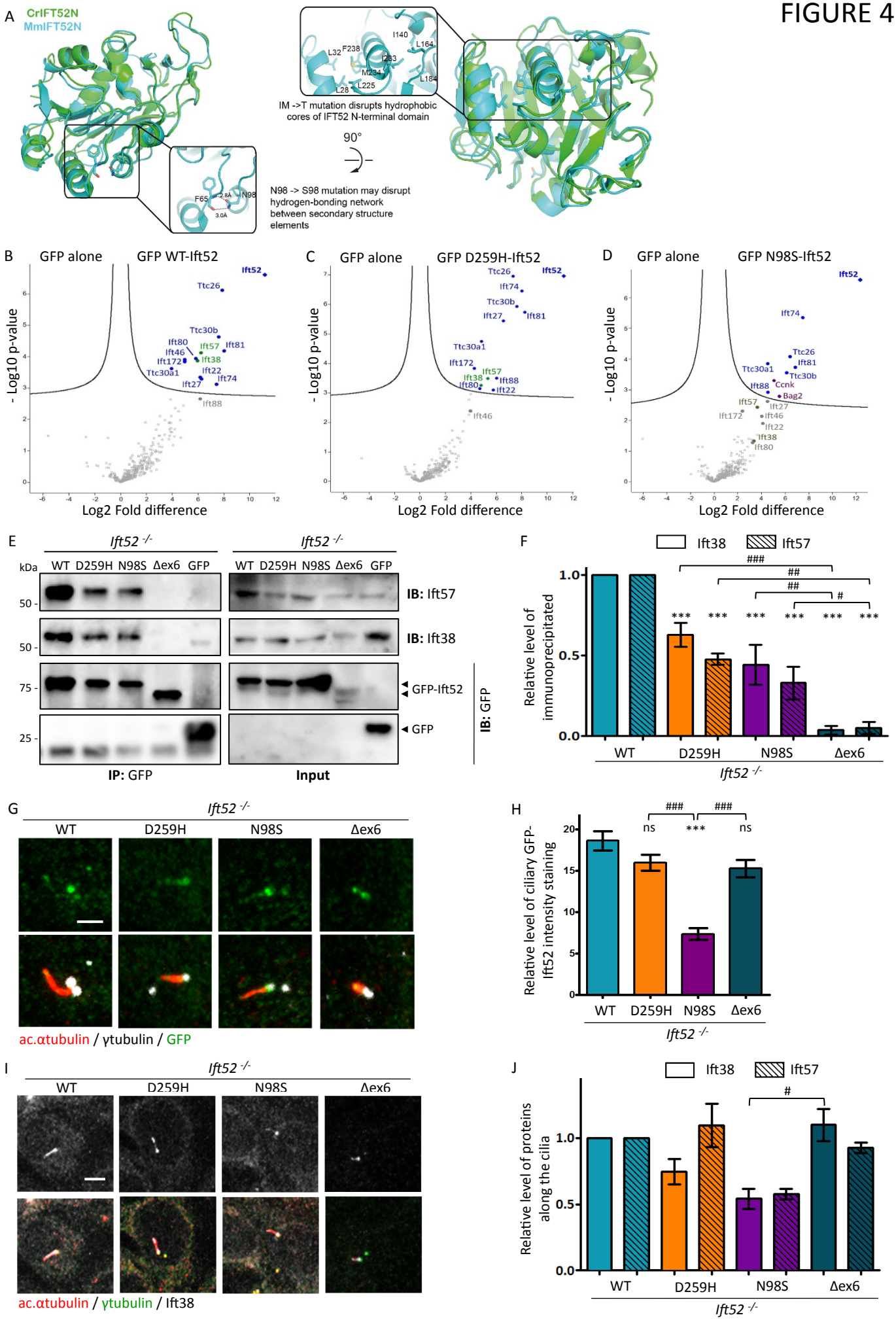
A
CrIFT52N
MmIFT52N
I140
L164
L32
F238
I233
M234
L184
L28
L225
IM ->T mutation disrupts hydrophobic cores of IFT52 N-terminal domain
90°
F65
2.8Å
N98
3.0Å
N98 -> S98 mutation may disrupt hydrogen-bonding network between secondary structure elements
B
GFP alone
GFP WT-Ift52
C
GFP alone
GFP D259H-Ift52
D
GFP alone
GFP N98S-Ift52
- Log10 p-value
Log2 Fold difference
Ift52
Ttc26
Ttc30b
Ift80
Ift46
Ift57
Ift81
Ift172
Ift38
Ttc30a1
Ift22
Ift27
Ift74
Ift88
Ttc30a1
Ift172
Ift57
Ift38
Ift88
Ift80
Ift22
Ift46
Ift74
Ttc26
Ift81
Ttc30b
Ccnk
Bag2
Ift57
Ift27
Ift172
Ift46
Ift22
Ift38
Ift80
E
Ift52 -/-
Ift52 -/-
kDa
WT D259H N98S Δex6 GFP
WT D259H N98S Δex6 GFP
50 -
50 -
75 -
25 -
IB: Ift57
IB: Ift38
GFP-Ift52
GFP
IB: GFP
IP: GFP
Input
F
Ift38
Ift57
Relative level of immunoprecipitated
1.0
0.5
0.0
###
##
##
#
***
WT
D259H
N98S
Δex6
Ift52 -/-
G
Ift52 -/-
WT
D259H
N98S
Δex6
ac.αtubulin / γtubulin / GFP
H
Relative level of ciliary GFP-Ift52 intensity staining
20
15
10
5
0
###
###
ns
***
ns
WT
D259H
N98S
Δex6
Ift52 -/-
I
Ift52 -/-
WT
D259H
N98S
Δex6
ac.αtubulin / γtubulin / Ift38
J
Ift38
Ift57
Relative level of proteins along the cilia
1.0
0.5
0.0
#
WT
D259H
N98S
Δex6
Ift52 -/-

FIGURE 5

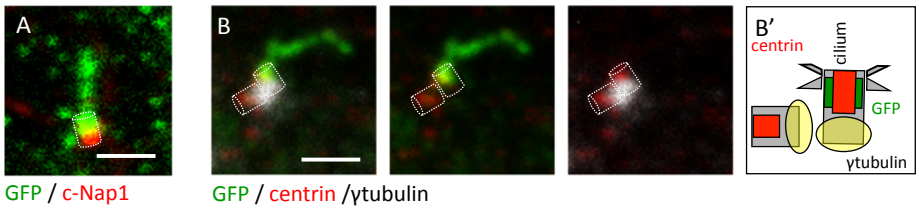
A
B
B'
centrin
cilium
GFP
γtubulin
GFP / c-Nap1
GFP / centrin /γtubulin

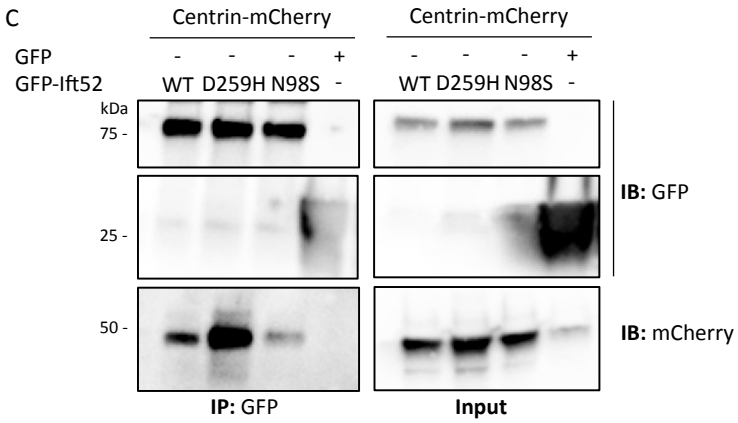
C
Centrin-mCherry
Centrin-mCherry
GFP
GFP-Ift52
WT D259H N98S
WT D259H N98S
kDa
75 -
25 -
50 -
IB: GFP
IB: mCherry
IP: GFP
Input

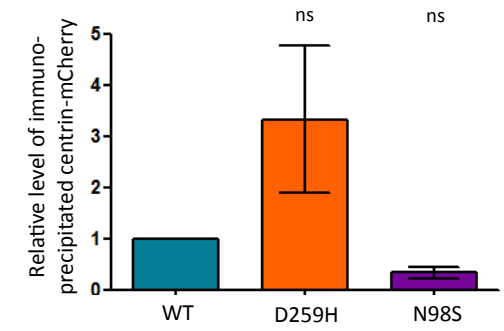
D
Relative level of immuno-precipitated centrin-mCherry
ns
ns
WT
D259H
N98S

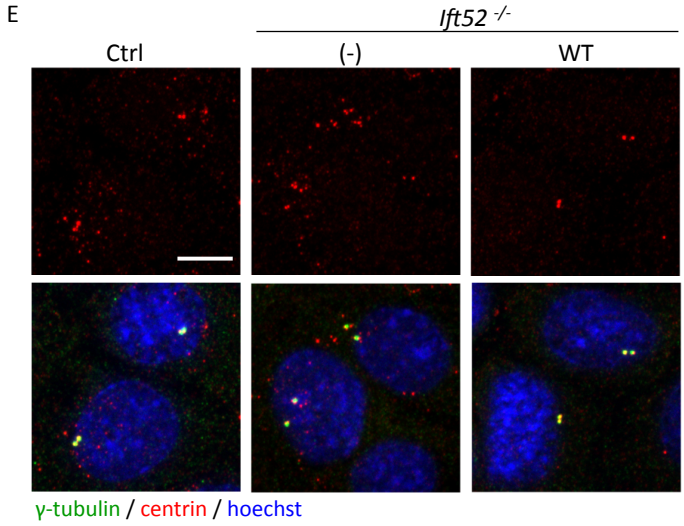
E
Ift52 -/-
Ctrl
(-)
WT
γ-tubulin / centrin / hoechst

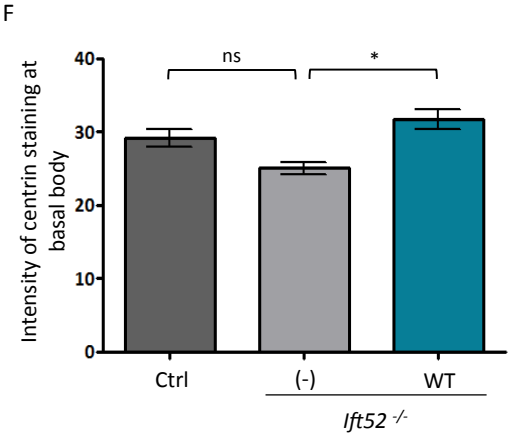
F
Intensity of centrin staining at basal body
ns
*
Ctrl
(-)
WT
Ift52 -/-

FIGURE 6

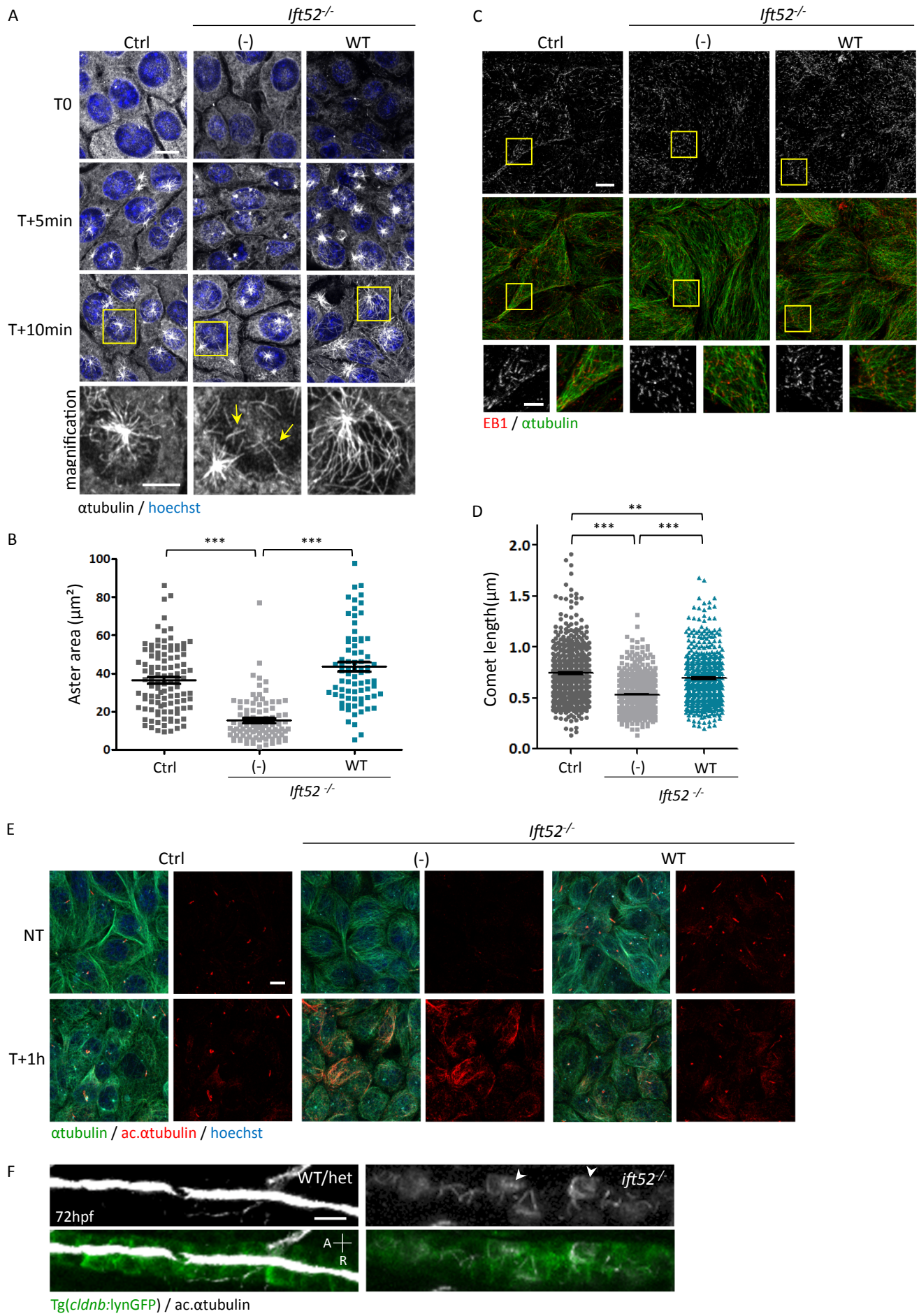
A
Ift52-/-
Ctrl
(-)
WT
T0
T+5min
T+10min
magnification
αtubulin / hoechst
C
Ift52-/-
Ctrl
(-)
WT
EB1 / αtubulin
B
Aster area (µm²)
***
***
Ctrl
(-)
WT
Ift52 -/-
D
Comet length(µm)
**
***
***
Ctrl
(-)
WT
Ift52 -/-
E
Ift52-/-
Ctrl
(-)
WT
NT
T+1h
αtubulin / ac.αtubulin / hoechst
F
WT/het
72hpf
ift52-/-
A
R
Tg(cldnb:lynGFP) / ac.αtubulin

FIGURE 7

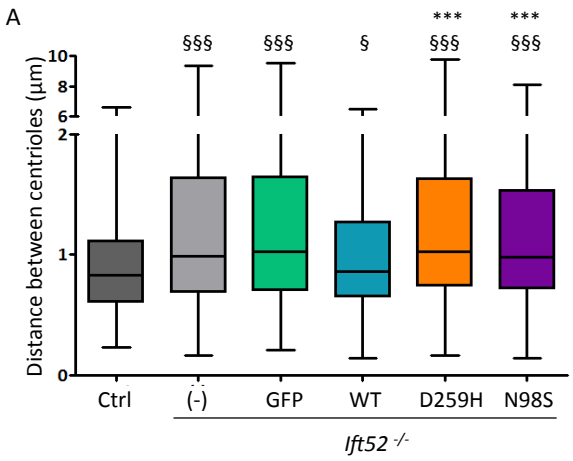
A
§§§
§§§
§
***
§§§
***
§§§
Distance between centrioles (µm)
10
8
6
2
1
0
Ctrl
(-)
GFP
WT
D259H
N98S
Ift52 -/-

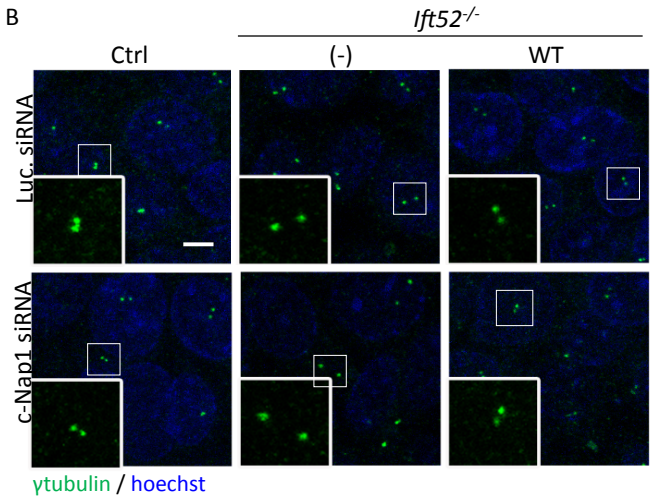
B
Ift52-/-
Ctrl
(-)
WT
Luc. siRNA
c-Nap1 siRNA
γtubulin / hoechst

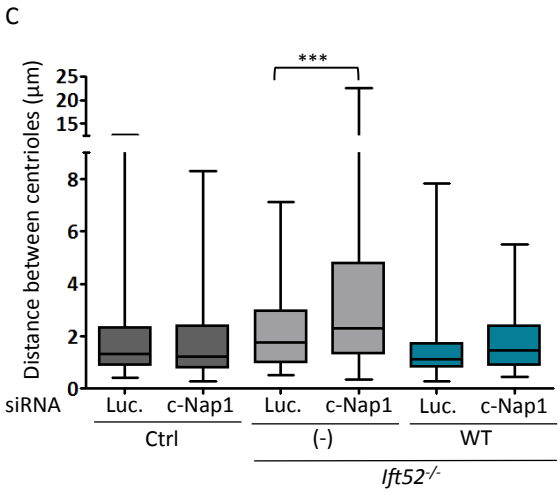
C
***
Distance between centrioles (µm)
25
20
15
8
6
4
2
0
siRNA
Luc.
c-Nap1
Luc.
c-Nap1
Luc.
c-Nap1
Ctrl
(-)
WT
Ift52-/-

Table S1 : Predicted pathogenicity and frequency of studied *IFT52* mutations

Nucleotide change[a]	Deduced protein change	PP2	SIFT	CADD	Variation	ExAC		GnomAD	
						Allele frequency	Allele count	Allele frequency	Allele count
c.775G>C	p.D259H	0	0.968	32	rs149821266	0.0004799	58/120852 (0 hom)	0.0003513	97/276110 (1 hom)
c.293A>G	p.N98S	0,027	0.999	25.2	rs530999984	0.00001652	2/121074 (0 hom)	8.297E-06	2/241054 (0 hom)
c.695-699delinsCA	p.I232M233delinsT	-	-	-	-	-	-	-	-
c.424C>T	p.R142*	-	-	37	rs748090019	0.00001649	2/121304 (0 hom)	8.13E-06	2/245998 (0 hom)

Abbreviations are as follows: PP2, polyphen2; SIFT, Sorting Intolerant From Tolerant; CADD, Combined Annotation Dependant Depletion; hom, homozygous.
[a]cDNA mutations are numbered according to human cDNA reference sequence GenBank:NM_016004.2 (IFT52), where +1 corresponds to the A of ATG start translation codon.

Table S2 : Filtered genes in F2:II-4 proband

Genomic position	Gene	Refseq Accession	nt change[a]	aa change	Zygosity	PP2	SIFT	CADD	Variation	ExAC	GnomAD
17:40,940,408	WNK4	NM_032387.4	c.2023C>T	p.R675W	hom	0.999	0	28.6	rs61755604	6/118860 (0 hom)	13/282370 (0 hom)
20:42,252,537	IFT52	NM_016004.2	c.775G>C	p.D259H	hom	0.96	0	32	rs149821266	58/120852 (0 hom)	97/276110 (1 hom)
20:44,444,310	UBE2C	NM_007019.2	c.347A>G	p.D116G	hom	0.928	0.01	25	No	No	No
2:114,429,470	AC017074.1 (ncRNA)	-	2:114429470_T>C	-	hom	-	-	0.9	No	No	No

Abbreviations are as follows: nt, nucleotide; aa, amino acid; PP2, polyphen2; SIFT, Sorting Intolerant From Tolerant; CADD, Combined Annotation Dependant Depletion; hom, homozygous; ncRNA, non coding RNA.
[a]cDNA mutations are numbered according to indicated human cDNA reference sequence GenBank, where +1 corresponds to the A of ATG start translation codon.

SUPP. FIGURE S1

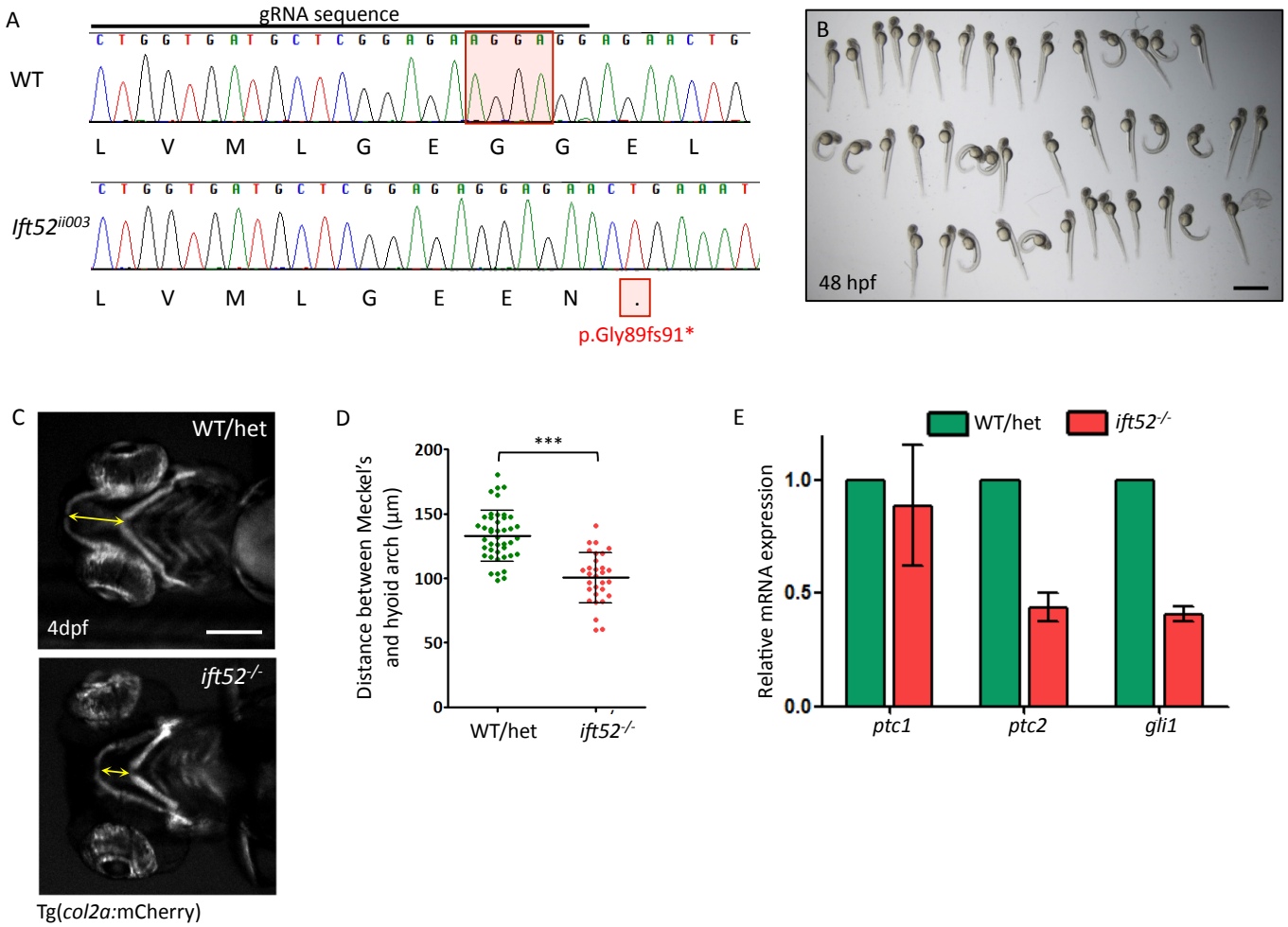

SUPP. FIGURE S2

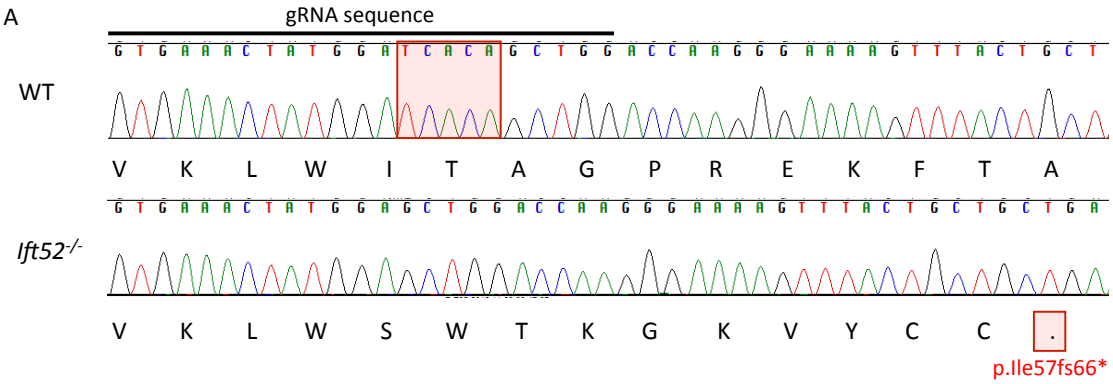

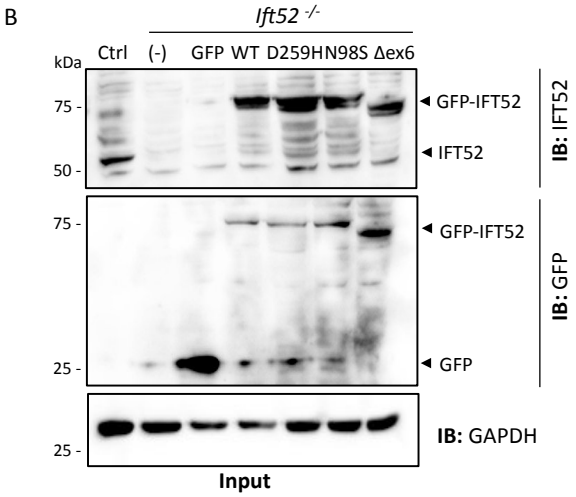

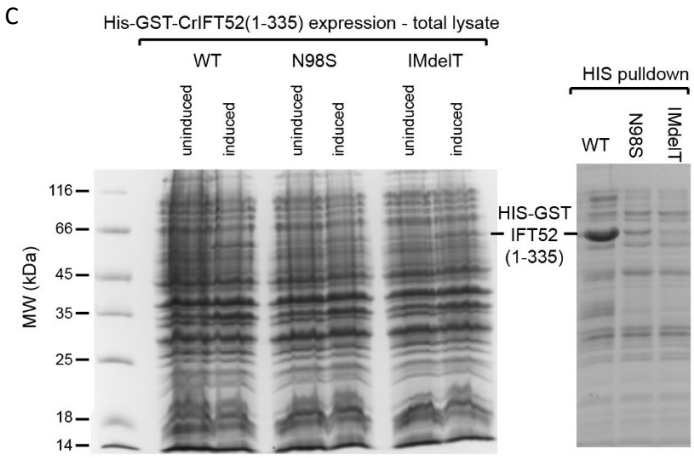

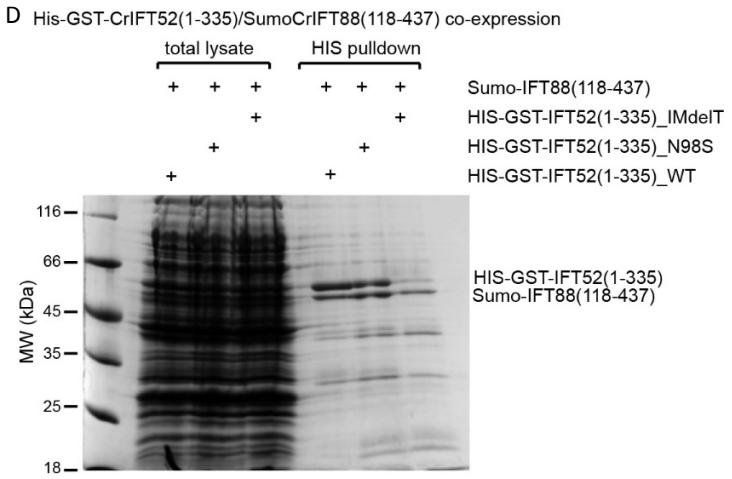

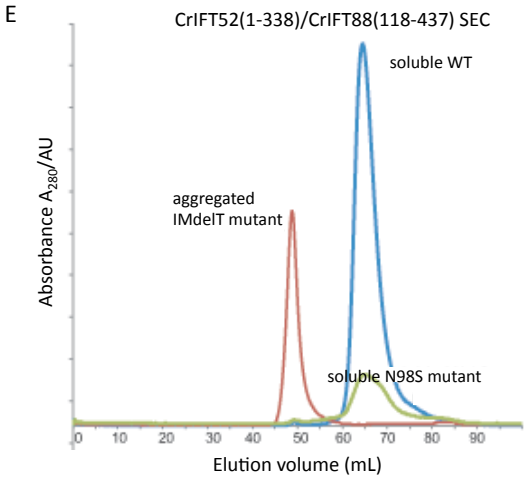

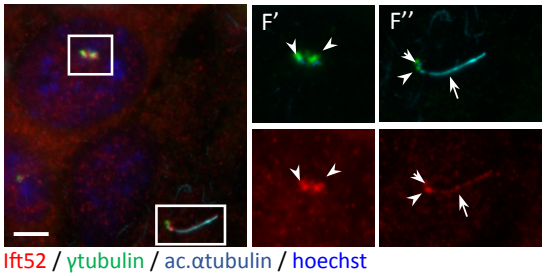

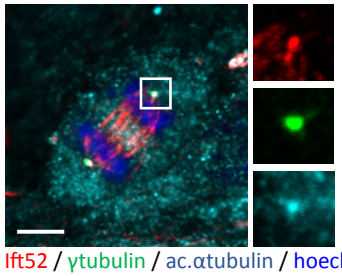

SUPP. FIGURE S3